Supporting Information

Investigating methane dry reforming on Ni and B promoted Ni surfaces: DFT assisted microkinetic analysis and addressing the coking problem

Ojus Mohan[a,b‡], Shambhawi[c‡], Alexei A. Lapkin[c,d*], and Samir H. Mushrif[b*]

[a] Energy Research Institute @NTU, Interdisciplinary Graduate School, Nanyang Technological University, 637335, Singapore
[b] Department of Chemical and Materials Engineering, University of Alberta, 9211-116 Street Northwest, Edmonton, Alberta T6G 1H9, Canada
[c] Department of Chemical Engineering and Biotechnology, University of Cambridge, Cambridge CB3 0AS, United Kingdom
[d] Cambridge Centre for Advanced Research and Education in Singapore Ltd, 1 Create Way, CREATE Tower #05-05, 138602, Singapore
**E-mail: aal35@cam.ac.uk (AL), mushrif@ualberta.ca (SHM)*
(‡ equal contribution authors)

KEYWORDS: density functional theory, dry reforming of methane, microkinetic study, reaction mechanism, coking, DRM

S1. NiB – Structure and stability

The location of boron promoter on nickel is explored by several computational and experimental studies by Xu et. al. [1–3]. They calculated the binding strength of boron on four on-surface sites present on nickel (top, bridge, fcc hollow, hcp hollow sites) and compared with the binding energy of boron on octahedral site present in first and second subsurface layer. The first subsurface octahedral site was found to be the most stable adsorption site for boron. This site is stable by 28 kJ/mol compared to the most stable on-surface site (hcp hollow site) and 20 kJ/mol more stable compared to the octahedral site in second subsurface layer. The stability of subsurface octahedral site is due to the strong bonding interaction between boron 2p and nickel 3d bands. The bonding orbital shifted to -4.8 eV for octahedral boron compared with -2.8 eV for on-surface boron. To test how boron filling happens, they studied boron binding energy for different configurations of four boron atoms on three adsorption sites (on-surface hollow site and octahedral sites in first and second subsurface layer). They found that a monolayer of boron in the first subsurface was the most stable configuration. In addition, the strong interaction between neighbouring boron atoms leads to the surface reconstruction of nickel atoms and it begins to resemble a stepped surface. Moreover, the surface reconstruction lowers the surface energy by 0.38 J/m^2 as compared to the plane surface. The NiB catalyst was successfully synthesized and characterized with 0.5% to 1% boron loading and also tested under steam reforming reaction conditions (800 ^{o}C, 1 atm). From XPS studies, it was observed that Ni:B ratio on surface was 1:0.64 compared to bulk ratio of 1:0.18 which clearly indicates that boron prefers surface sites compared to the bulk. Importantly, the presence of sub-surface B prevents the diffusion of carbon to the bulk and sub-surface sites in Ni. Based on scanning electron microscopy (SEM) and temperature-programmed oxidation (TPO), it was shown that the amount of deposited carbon reduced by 80%[2]. The structures of NiB before and after optimization is shown in Figure S1.

To test the stability at high pressure (10 atm), we evaluated the Gibbs free energy change of the reaction:

$$\frac{n}{2}B_2H_{6\ (gas)} + Ni \rightarrow NiB_n + \frac{3n}{2}H_{2\ (gas)}$$

under 1atm and 10 atm pressures. This method is widely employed to assess the stabilities of boron promoted transition metals (Cu-B [4], Ni-B [3] and Pd-B[5]. Diborane (B_2H_6) is used as the source of boron as it is more stable than boric acid (H_3BO_3) under the reaction conditions. We found that the difference in Gibbs free energy change for the reaction (A) at 1 atm pressure and 10 atm pressure (temperature is kept same at 973 K) is only 1.5 kJ/mol. This clearly indicates that increasing the pressure to 10 atm doesn't affect the stability of NiB.

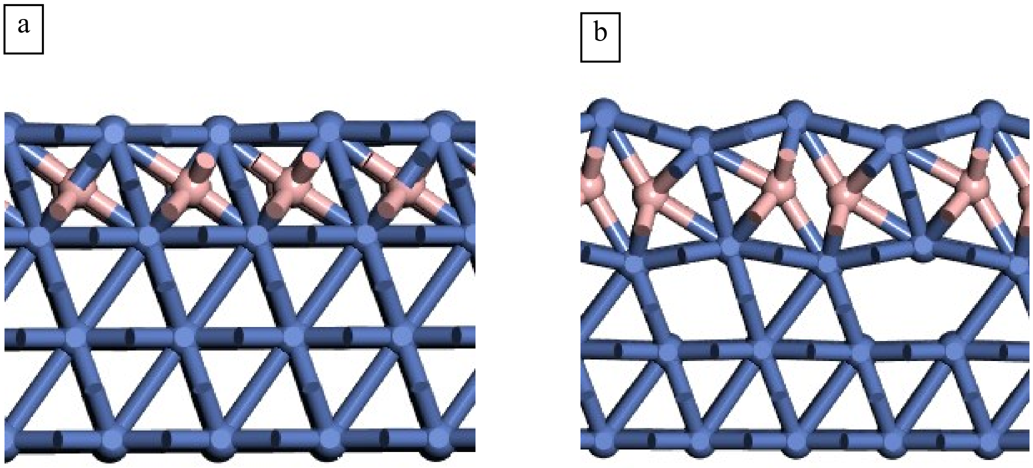

Figure S1. The structure of NiB a) before optimization b) after optimization. Blue and salmon colour represents nickel and boron respectively.

S2. Estimating rate constants and Gibbs energy for elementary reaction steps

The rate constants of each reaction step are determined using the transition state theory[6]

$$k = k_B T/h \, exp\left[\frac{-\Delta G_{act}}{RT}\right] \tag{1}$$

where, ΔG_{act} is the Gibbs free energy of activation of the reaction step and R is the universal gas constant.

Once the forward rate constant (k_f) is known, the backward rate constant (k_r) could be derived using the equilibrium constant (K_{eq})

$$\frac{k_f}{k_r} = K_{eq} = exp\left[\frac{-\Delta G_{rec}}{RT}\right] \tag{2}$$

where, ΔG_{rec} is the Gibbs free energy of the reaction step. Given an elementary reaction step with transition state species $AB_{\#}$
$A + B \leftrightarrow AB_{\#} \leftrightarrow C + D$
ΔG_{act} and ΔG_{rec} is defined as

$$\Delta G_{act} = G_{AB_{\#}} - G_A - G_B \tag{3}$$

$$\Delta G_{rec} = G_C + G_D - G_A - G_B \tag{4}$$

The Gibbs energy (G_A) for a species is given as

$$G_A = E_{DFT} + E_{ZPE} + \Delta H_T(0 \rightarrow T) - T\Delta S \qquad (5)$$

where, E_{DFT} is the energy obtained from DFT, E_{ZPE} is the zero point energy correction, ΔH_T is the temperature correction from 0 K to the reaction temperature T and $T\Delta S$ is the entropy correction. The zero point energy correction is calculated as

$$E_{ZPE} = \sum_{i=1}^{\#\,of\,modes} \frac{N_A h\vartheta_i}{2} \qquad (6)$$

where, N_A is Avogadro's number, h is Planck's constant and ϑ_i is the frequency of the normal mode. However, temperature and entropy corrections are different for gaseous and surface species[6,7].

Gaseous species

These species have all of the translational, rotational and vibrational degrees of freedom active. Hence total enthalpy temperature correction ΔH_T at temperature T is given as sum of translational (H_{trans}), rotational (H_{rot}) and vibrational (H_{vib}) enthalpy corrections

$$\Delta H_T = H_{trans} + H_{rot} + H_{vib} \qquad (7)$$

where,

$$H_{trans} = \frac{5}{2}RT \qquad (8)$$

$$H_{rot} = \frac{f}{2}RT \qquad (9)$$

f is equal to 2 for linear molecules and 3 for other cases

$$H_{vib} = \sum_{i}^{\#\,of\,modes} \frac{N_A h v_i e^{-hv_i/k_BT}}{1 - e^{-hv_i/k_BT}} \qquad (10)$$

k_B is the Boltzmann constant

Similarly, the total entropy correction is given as the sum of translational ($S_{trans,3D}$), rotational (S_{rot}) and vibrational (S_{vib}) entropy corrections

$$\Delta S = S_{trans,3D} + S_{rot} + S_{vib} \qquad (11)$$

The translational entropy correction is given as

$$S_{trans,3D} = R\left[ln\left(\frac{(2\pi m k_B T)^{\frac{3}{2}}}{h^3}\right) + ln\left[\frac{V}{N_g}\right] + \frac{5}{2}\right] \tag{12}$$

where m is the mass of the molecule and $\frac{V}{N_g}$ is the volume per molecule in the standard state. The rotational entropy correction for a non-linear molecule is given as

$$S_{rot} = R\left[ln\left(\frac{8\pi^2\sqrt{8\pi^3 I_{x1}I_{x2}I_{x3}(k_B T)^{\frac{3}{2}}}}{\sigma_r h^3}\right) + \frac{3}{2}\right] \tag{13}$$

where I_{x1}, I_{x2}, and I_{x3} are the three moments of inertia about the principal axes and σ_r is the rotational symmetry number. For linear molecules however

$$S_{rot,\,linear} = R\left[ln\left(\frac{8\pi^2 I_{linear}(k_B T)}{\sigma_r h^2}\right) + 1\right] \tag{14}$$

Where I_{linear} is the moment of inertia of the linear molecule. The vibrational entropy correction of a molecule is

$$S_{vib} = R\sum_{i}^{\#\,of\,modes}\left(\frac{\frac{hv_i}{k_B T}}{e^{hv_i/k_B T} - 1} - ln\left(1 - e^{-hv_i/k_B T}\right)\right) \tag{15}$$

For the gas phase species at reaction temperature T and pressure P, we also include pressure corrections $\left(S_p = RT\ln\left(\frac{P}{P^0}\right)\right)$ in the right hand side of equation (5) for computing Gibbs energy.

Weakly bound species

The weakly bound species such as physisorbed CO_2 are treated as 2D gases that maintain the full rotational and vibrational modes of their corresponding 3D gaseous species. Therefore, temperature and entropy corrections corresponding to rotation and vibration are the same as for the gaseous species. However, the translational correction terms at temperature T are given as

$$H_{trans,2D} = 2RT \tag{16}$$

$$S_{trans,2D} = R\left[ln\left(\frac{2\pi m k_B T}{h^2}\right) + ln\left(\frac{SA}{N_{sat}}\right) + 2\right] \tag{17}$$

where, $\frac{SA}{N_{sat}}$ is the area occupied per adsorbed molecule at the standard state conditions which is equal to the reciprocal of the surface concentration for monolayer coverage.

Tightly bound species

All of the intermediate and transition state species are tightly bound species. Since they are bonded to the surface their translational and rotational modes are replaced by vibrational modes corresponding to frustrated translation and rotation on the surface. Their temperature and entropy corrections are given using the same equation (10) and (15).

It should be noted that we do not include these corrections while computing Gibbs energy of the lattice as they anyway get cancelled while computing activation and reaction energies.

For computing the rate constants of the adsorption and the desorption reactions, both transition state theory and collision theory can be applied. However, it is known that the expression for the rate of adsorption obtained from collision theory with σ = 1 is the same as that obtained from transition state theory for a mobile activated complex with E_a(T = 0) = 0[6]. Therefore, in this study, the rate constants (k_{ads}) for adsorption reactions are also computed using the transition state theory [8].

$$k_{ads} = \sigma k_B T/h \, exp\left[\frac{-\Delta G_{act}}{RT}\right] \tag{18}$$

where, σ is the sticking coefficient. The sticking coefficients for NiB is assumed to be same as that of Ni (110). The corresponding sticking coefficients for Ni (111) and Ni (110) is obtained from literature [8].

Table S1. Activation barriers and reaction energies (electronic energy) of all elementary reactions for DRM on Ni (111) and NiB surfaces.

Reaction	Activation barrier (kJ/mol)			Reaction energy (kJ/mol)	
	Ni (111)		NiB	Ni (111)	NiB
	Current work	Reported			
R1: $CH_4^* \rightarrow CH_3^* + H^*$	115	112[8],118[9], 112[10], 129[11,12]	91	43	25

R2: $CH_3^* \rightarrow CH_2^* + H^*$	75	78[8], 81[9], 79[10], 66[9]	86	17	68
R3: $CH_2^* \rightarrow CH^* + H^*$	35	35[8], 28[9], 36[10], 26[9]	53	-32	15
R4: $CH^* \rightarrow C^* + H^*$	137	138[13], 132[10], 135[9]	106	47	61
R5: $CO_2^* \rightarrow CO^* + O^*$	54	64[7], 43[14], 39[15], 53[10]	124	-113	-40
R6: $CO_2^* + H^* \rightarrow COOH^*$	109	108[7], 99[14]	140	5	9
R7: $CO_2^* + H^* \rightarrow HCOO^*$	67	52[14], 56[15]	63	-48	-82
R8: $COOH^* \rightarrow CO^* + OH^*$	37	54[7], 36[15]	87	-107	-94
R9: $HCOO^* \rightarrow HCO^* + O^*$	148	134[15]	230	46	123
R10: $HCO^* \rightarrow CO^* + H^*$	30	19[7], 28[10], 20[9]	38	-111	-82
R11: $COOH^* + H^* \rightarrow HCOOH^*$	83	-	84	16	16
R12: $HCOO^* + H^* \rightarrow HCOOH^*$	127	77[14]	154	70	106
R13: $HCOOH^* \rightarrow HCO^* + OH^*$	100	86[14]	80	-12	-28
R14: $CH_3OH^* \rightarrow CH_2OH^* + H^*$	119	84[7]	102	35	36
R15: $CH_2OH^* \rightarrow CHOH^* + H^*$	74	51[7]	92	-7	41
R16: $CHOH^* \rightarrow COH^* + H^*$	27	14[7]	67	-58	20
R17: $COH^* \rightarrow CO^* + H^*$	101	94[7], 86[9]	88	-101	-153
R18: $CH_3^* + OH^* \rightarrow CH_3OH^*$	197	211[7], 174[16], 125[9]	216	38	55
R19: $CH_2^* + OH^* \rightarrow CH_2OH^*$	132	126[7], 85[9]	89	57	23
R20: $CH^* + OH^* \rightarrow CHOH^*$	154	142[7], 138[16], 123[9]	145	82	49
R21: $C^* + OH^* \rightarrow COH^*$	149	140[7], 126[9]	137	-24	8
R22: $CH_3O^* \rightarrow CH_2O^* + H^*$	113	89[7], 62[10]	93	52	49
R23: $CH_2O^* \rightarrow CHO^* + H^*$	50	34[7], 37[10]	54	-20	-2
R24: $CH_3^* + O^* \rightarrow CH_3O^*$	133	152[7], 90[10],	158	-1	-9

		152[9]			
R25: $CH_2^*+O^* \rightarrow CH_2O^*$	130	139[7], 75[10], 131[9]	101	34	-29
R26: $CH^*+O^* \rightarrow CHO^*$	145	146[7], 77[10], 108[16], 151[9]	168	45	-46
R27: $C^*+O^* \rightarrow CO^*$	162	152[7], 206[9]	170	-113	-189
R28: $CH_3OH^*+^* \rightarrow CH_3O^*+H^*$	101	-	100	51	-20
R29: $CH_2OH^*+^* \rightarrow CH_2O^*+H^*$	76	-	110	-34	-7
R30: $CHOH^*+^* \rightarrow HCO^*+H^*$	83	-	70	-48	-51
R31: $O^*+H^* \rightarrow OH^*$	125	129[7], 128[10]	119	12	-44
R32: $OH^*+H^* \rightarrow H_2O^*$	147	137[10]	137	56	64
R33: $H^*+H^* \rightarrow H_2$	86	81[17]	68	58	38
R34: $OH^*+OH^* \rightarrow H_2O^*+O^*$	92	-	106	44	109
R35: $CO_2^*+C^* \rightarrow 2CO^*$	153	-	123	-226	-229
R36: $CO_2 \rightarrow CO_2^*$	-	-	-	-17	-61
R37: $CO^* \rightarrow CO$	-	-	-	148	144
R38: $H_2O^* \rightarrow H_2O + ^*$	-	-	-	30	60

Table S2. Kinetic rate constants of elementary reactions.

Elementary reactions	Rate Constants (s^{-1})			
	Ni (111)		B-doped Ni	
	k_f	k_r	k_f	k_r
R1: $CH_4*\rightarrow CH_3*+H*$	$1.65\text{x}10^{2}$	$8.58\text{x}10^{8}$	$1.40\text{x}10^{5}$	$3.23\text{x}10^{10}$
R2: $CH_3*\rightarrow CH_2*+H*$	$1.4\text{x}10^{10}$	$2.46\text{x}10^{10}$	$3.84\text{x}10^{8}$	$9.25\text{x}10^{11}$
R3: $CH_2*\rightarrow CH*+H*$	$2.49\text{x}10^{11}$	$1.08\text{x}10^{10}$	$1.95\text{x}10^{10}$	$1.01\text{x}10^{11}$
R4: $CH*\rightarrow C*+H*$	$3.15\text{x}10^{6}$	$5.01\text{x}10^{8}$	$1.27\text{x}10^{8}$	$1.15\text{x}10^{11}$
R5: $CO_2*\rightarrow CO*+O*$	$7.84\text{x}10^{9}$	$2.90\text{x}10^{4}$	$3.15\text{x}10^{7}$	$7.68\text{x}10^{4}$
R6: $CO_2*+H*\rightarrow COOH*$	$1.66\text{x}10^{7}$	$6.5\text{x}10^{8}$	$3.86\text{x}10^{5}$	$9.87\text{x}10^{6}$
R7: $CO_2*+H*\rightarrow HCOO*$	$3.8\text{x}10^{9}$	$3.71\text{x}10^{8}$	$1.03\text{x}10^{10}$	$1.18\text{x}10^{7}$
R8: $COOH*\rightarrow CO*+OH*$	$7.64\text{x}10^{12}$	$2.66\text{x}10^{6}$	$1.21\text{x}10^{10}$	$4.20\text{x}10^{3}$
R9: $HCOO*\rightarrow HCO*+O*$	$2.09\text{x}10^{5}$	$5.34\text{x}10^{7}$	$1.26\text{x}10^{1}$	$1.60\text{x}10^{7}$
R10: $HCO*\rightarrow CO*+H*$	$3.27\text{x}10^{12}$	$4.86\text{x}10^{5}$	$3.95\text{x}10^{12}$	$6.65\text{x}10^{6}$
R11: $COOH*+H*\rightarrow HCOOH*$	$6.94\text{x}10^{8}$	$2.9\text{x}10^{9}$	$3.09\text{x}10^{8}$	$8.5\text{x}10^{9}$
R12: $HCOO*+H*\rightarrow HCOOH*$	$4.65\text{x}10^{7}$	$7.77\text{x}10^{10}$	$1.34\text{x}10^{6}$	$8.31\text{x}10^{11}$
R13: $HCOOH*\rightarrow HCO*+OH*$	$7.94\text{x}10^{9}$	$4.45\text{x}10^{9}$	$2.73\text{x}10^{9}$	$2.04\text{x}10^{7}$
R14: $CH_3OH*\rightarrow CH_2OH*+H*$	$3.98\text{x}10^{5}$	$6.86\text{x}10^{8}$	$1.63\text{x}10^{7}$	$4.20\text{x}10^{9}$
R15: $CH_2OH*\rightarrow CHOH*+H*$	$2.77\text{x}10^{9}$	$2.47\text{x}10^{8}$	$2.43\text{x}10^{9}$	$1.03\text{x}10^{10}$
R16: $CHOH*\rightarrow COH*+H*$	$1.61\text{x}10^{12}$	$3.13\text{x}10^{8}$	$6.05\text{x}10^{9}$	$5.54\text{x}10^{10}$
R17: $COH*\rightarrow CO*+H*$	$8.44\text{x}10^{7}$	$7.85\text{x}10^{1}$	$2.75\text{x}10^{9}$	$8.72\text{x}10^{-1}$
R18: $CH_3*+OH*\rightarrow CH_3OH*$	$3.13\text{x}10^{3}$	$2.90\text{x}10^{4}$	$3.34\text{x}10^{1}$	$8.60\text{x}10^{4}$

R19: CH_2*+OH*→CH_2OH*	$1.31x10^{6}$	$1.19x10^{10}$	$1.76x10^{8}$	$4.86x10^{10}$
R20: CH*+OH*→ CHOH*	$8.41x10^{5}$	$1.57x10^{10}$	$2.70x10^{5}$	$6.12x10^{7}$
R21: C*+OH*→COH*	$1.34x10^{6}$	$3.04x10^{4}$	$6.70x10^{5}$	$1.53x10^{6}$
R22: CH_3O*→CH_2O*+H*	$6.21x10^{7}$	$1.84x10^{10}$	$3.00x10^{8}$	$5.38x10^{10}$
R23: CH2O*→CHO*+H*	$2.86x10^{11}$	$2.98x10^{9}$	$8.96x10^{10}$	$1.66x10^{10}$
R24: CH_3*+O* →CH_3O*	$1.78x10^{6}$	$3.70x10^{6}$	$1.38x10^{5}$	73429.8
R25: CH_2*+O*→CH_2O*	$1.54x10^{6}$	$5.34x10^{8}$	$5.78x10^{7}$	$2.29x10^{6}$
R26: CH*+O*→ CHO*	$4.18x10^{5}$	$3.49x10^{7}$	$6.22x10^{4}$	$8.86x10^{1}$
R27: C*+O*→CO*	$7.44x10^{4}$	$5.78x10^{-3}$	$5.03x10^{4}$	$1.33x10^{-7}$
R28: CH_3OH*+*→ CH_3O*+H*	$1.21x10^{8}$	$7.28x10^{6}$	$3.94x10^{8}$	$2.24x10^{7}$
R29: CH_2OH*+*→ CH_2O*+H*	$3.55x10^{9}$	$3.67x10^{7}$	$1.33x10^{8}$	$5.24x10^{6}$
R30: CHOH*+*→ HCO*+H*	$1.73x10^{10}$	$2.10x10^{7}$	$2.54x10^{9}$	$4.37x10^{6}$
R31: O*+H*→OH*	$1.35x10^{7}$	$4.97x10^{7}$	$1.03x10^{7}$	$3.74x10^{4}$
R32: OH*+H*→H_2O*	$3.45x10^{6}$	$3.49x10^{7}$	$5.76x10^{6}$	$3.56x10^{7}$
R33: H*+H*→H_2	$3.45x10^{8}$	$2.65x10^{6}$	$7.81x10^{8}$	$9.62x10^{5}$
R34: OH*+OH*→H_2O*+O*	$3.3x10^{8}$	$9.11x10^{8}$	$1.61x10^{7}$	$2.73x10^{10}$
R35: CO_2*+C*→2CO*	$1.00x10^{5}$	$2.88x10^{-8}$	$1.55x10^{6}$	$1.00x10^{-8}$
R36: CO_2→CO_2*	$1.18x10^{2}$	$2.48x10^{7}$	$1.77x10^{3}$	$2.39x10^{6}$
R37: CO*→CO	$3.67x10^{5}$	$8.21x10^{6}$	$1.40x10^{6}$	$7.80x10^{7}$
R38: H_2O* →H_2O + *	$2.84x10^{11}$	$2.01x10^{8}$	$7.45x10^{9}$	$1.34x10^{8}$

S3. Model development and comparison

Herein we re-compute the results of the previously reported model [18] for the DRM reaction over Ni. We then develop a series of models by varying the number of elementary reaction steps and the DFT corrections used (See Table S3) to finally develop our microkinetic model (Model 4) i.e. the most comprehensive model (See section 2.2, Table 1).

Table S3. Different model specifications

Specification	Reported model	Model 1	Model 2	Model 3	Model 4
DFT functional	PBE [19]	PBE	PBE	rPBE-vdW [20]	rPBE-vdW
Dispersion correction	No	No	No	Yes	Yes
Number of elementary steps	33	33	33	33	38
P_{std}	1 Pa	1 Pa	10^5Pa	10^5Pa	10^5Pa

It should be noted that the previously reported kinetic rate constants[18] were directly employed in Models 1 and 2. The following five extra reactions were included in Model 4 apart from the 33 reactions in the reported model[18]

I. $COOH^*+H^* \rightarrow HCOOH^*$
II. $HCOO^*+H^* \rightarrow HCOOH^*$
III. $HCOOH^* \rightarrow HCO^* + OH^*$
IV. $OH^*+OH^* \rightarrow H_2O^*+O^*$
V. $CO_2^*+C^* \rightarrow 2CO^*$

The models were solved for the reaction conditions adapted from section 3.2.1 in the paper. The surface coverages of reaction intermediates obtained after solving these microkinetic models are given in Table S4.

Table S4. Fractional surface coverages of surface species over Ni computed by different models at a reaction temperature of 973.15 K, 10 bar pressure and an inlet feed composition of 50% volume fraction CH_4 and 50% volume fraction of CO_2. Model 1 and 2 uses PBE DFT functional and it does not include dispersion corrections. Model 3 and 4 uses rPBE-vdW DFT functional that includes dispersion corrections

Species	Reported[18]	Model 1	Model 2	Model 3	Model 4
CH_3^*	9.98×10^{-7}	9.98×10^{-7}	5.99×10^{-12}	1.02×10^{-7}	9.71×10^{-8}
CH_2^*	3.21×10^{-6}	3.49×10^{-6}	8.81×10^{-14}	7.85×10^{-7}	7.58×10^{-7}
CH^*	1.19×10^{-3}	1.41×10^{-3}	2.76×10^{-9}	2.49×10^{-4}	2.46×10^{-4}
C^*	1.69×10^{-2}	1.64×10^{-1}	4.34×10^{-4}	2.15×10^{-5}	2.17×10^{-5}

CO_2*	4.89x10^{-6}	4.61x10^{-6}	3.44x10^{-10}	1.02x10^{-6}	1.02x10^{-6}
CO*	6.60x10^{-1}	5.50x10^{-1}	6.81x10^{-7}	9.24x10^{-1}	9.25x10^{-1}
COOH*	6.47x10^{-10}	4.47x10^{-10}	3.91x10^{-20}	1.88x10^{-9}	1.84x10^{-9}
HCOO*	3.78x10^{-8}	1.18x10^{-10}	2.13x10^{-19}	7.6x10^{-7}	7.43x10^{-7}
HCO*	3.72x10^{-8}	2.85x10^{-8}	2.73x10^{-17}	9.93x10^{-9}	9.78x10^{-9}
HCOOH*	-	-	-	-	3.16x10^{-11}
CH_3OH*	3.20x10^{-15}	1.94x10^{-15}	2.06x10^{-26}	4.56x10^{-12}	4.21x10^{-12}
CH_2OH	3.82x10^{-14}	2.67x10^{-14}	6.9x10^{-27}	3.34x10^{-13}	3.14x10^{-13}
CHOH*	4.11x10^{-12}	2.95x10^{-12}	8.34x10^{-24}	1.84x10^{-12}	1.76x10^{-12}
COH*	2.09x10^{-7}	1.62x10^{-7}	4.43x10^{-16}	7.83x10^{-8}	7.66x10^{-8}
CH_3O*	1.50x10^{-11}	9.84x10^{-12}	1.02x10^{-19}	1.01x10^{-9}	9.52x10^{-10}
CH_2O*	1.36x10^{-11}	9.62x10^{-12}	6.64x10^{-22}	8.93x10^{-12}	8.61x10^{-12}
H_2O*	2.66x10^{-6}	2.27x10^{-6}	5.64x10^{-13}	1.22x10^{-6}	2.08x10^{-6}
O*	2.40x10^{-3}	2.43x10^{-3}	9.61x10^{-4}	1.65x10^{-2}	1.605x10^{-2}
H*	5.71x10^{-2}	4.69x10^{-2}	1.48x10^{-4}	4.02x10^{-3}	3.84x10^{-3}
OH*	6.13x10^{-5}	5.69x10^{-5}	1.68x10^{-8}	3.25x10^{-4}	3.09x10^{-4}
Free Site (*)	2.63x10^{-1}	2.35x10^{-1}	9.98x10^{-1}	5.53x10^{-2}	5.41x10^{-2}
x_{CH_4}	1.59x10^{-1}	1.44x10^{-1}	2.2x10^{-3}	7.69x10^{-2}	7.67x10^{-2}
x_{CO_2}	3.78x10^{-1}	3.51x10^{-1}	3.26x10^{-3}	8.36x10^{-2}	8.84x10^{-2}

From Table S4 it may be concluded that Model 1 has successfully reproduced the reported values of fractional coverages. However, the correct value of P_{std}, i.e. 10^5 Pa, is not employed in the adsorption rate equations (Equation 2) for this model, instead a value of 1 Pa is assumed. Therefore, in order to correctly employ P_{std} in the rate equations, Model 2 is constructed and although Model 1 closely resembles the reported study[18], the surface coverage obtained from Model 2 is considered for further analysis.

Model 3, on the other hand, is constructed from the energy data generated by DFT calculation using appropriate functional and corrections. After incorporating these corrections, we can see that the surface coverages of the adsorbed reactant is significantly improved. The fractional surface coverage of CH_3* and CO_2* have increased from 5.99x10^{-12} to 1.02x10^{-7} and 3.44x10^{-10} to 1.02x10^{-6} respectively. The fractional coverage of free site (*) has also decreased notably from 9.98x10^{-1} to 5.53x10^{-2} demonstrating the requirement of accurate DFT functional and corrections in microkinetic modeling.

Furthermore, the surface coverage values obtained by Model 3 indicate that the catalyst surface is mostly covered by CO* and there is a high possibility of the occurrence of Boudouard reaction. Hence, to accurately model the whole reaction system, we constructed the most elaborate model, Model 4, by including all relevant elementary reactions from the literature [7,8,21–23] in our further analysis.

From the results in Table S4, we can conclude that including more elementary reaction steps did not affect the fractional surface coverages values on Ni (111) surface significantly. Yet we employ Model 4 to perform microkinetic analysis on Boron-doped Ni as it is a different catalyst surface. A more comprehensive model has better chances of predicting accurate results over a new catalyst surface, moreover, the forward rate constant of Boudouard reaction (R35), is significantly higher on B-doped Ni than on Ni.

S4. Model Assessment of the most comprehensive model (Model 4)

The results obtained from the model are compared with the experimental data [24] and data from the previously reported model [18]. We ensured the validity of our Model 4 (see Table S3) by analysing the (i) CH_4 fraction conversion vs space-time (W/F_0) curves at different temperatures (Figure S2) and (ii) exit concentration values of reactants (CH_4 and CO_2) and products (CO and H_2) vs temperature curves (Figure S3) and comparing our results with previously reported study [18] .

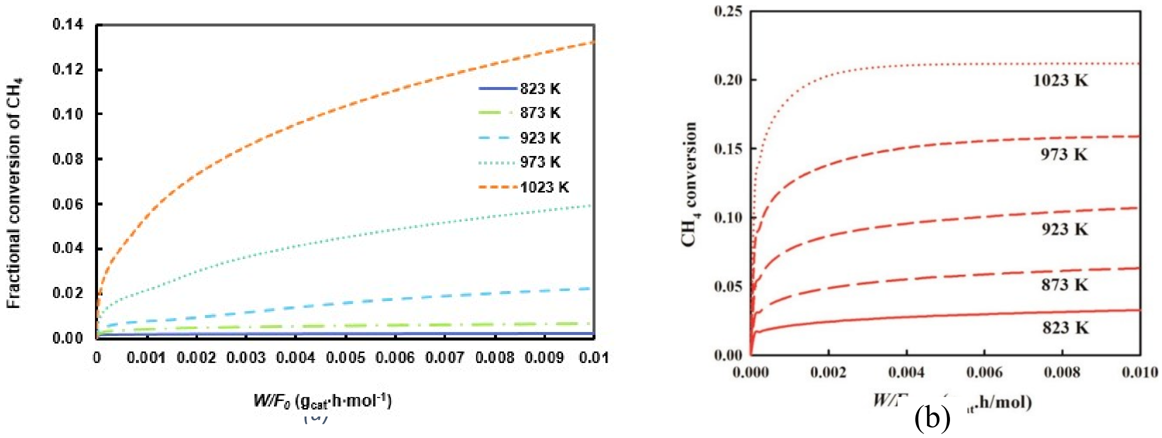

Figure S2. CH_4 fractional conversion vs W/F_0 (g_{cat}·h·mol^{-1}) (a) predicted by Model 4 and (b) reported [18] at various reaction temperature and a pressure of 10 bar

From Figure S2, we observe that the reactant conversion increases as the space time increases and higher reactant conversions are achieved at greater reaction temperatures. This observation is in agreement with the previously reported study [18]. The CH_4 conversion increases from ~0.2% at 823 K to ~ 13.2% at 1023 K. This increase is within good quantitative agreement of that observed in the previous model where conversion increases from ~2% at 823 K to 20% at 1023 K. However, the fractional conversion values are quite different from the reported values due to the varying model specification. More details can be found in Table S3.

We further compared the fractional conversion results, as predicted from the Model 4 with experimental data [24], in terms of the exit concentration values of reactants (CH_4 and CO_2) and products (CO and H_2). The results are shown in Figure S3.

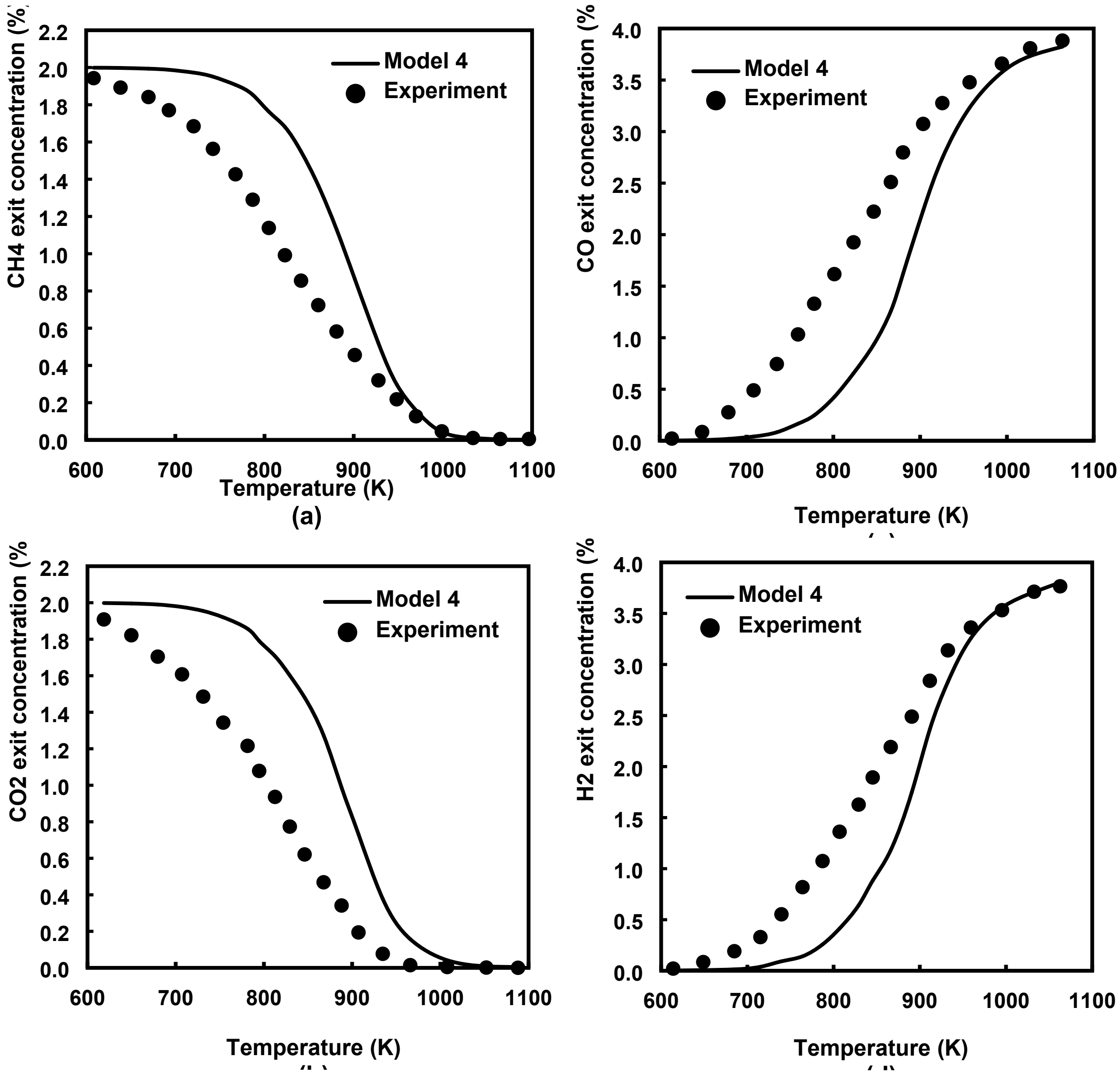

Figure S3. Comparison of the experimentally observed[24] (circles) and the numerically predicted (lines) exit concentrations (%) of (a) CH_4, (b) CO_2 (c) CO and (d) H_2 as a function of temperature for dry reforming of methane.

As observed from Figure S3, the exit concentration of reactants decreases and products increases as temperature increases. This is in accordance with experiments. Moreover, at reaction temperature above 923 K, the value of exit concentrations of both reactants and products are in good agreement with the experimental values. However, as the temperature decreases, the model over predicts the reactant exit concentration (Figure S3 (a) and (b)) and under predicts the product exit concentration (Figure S3 (c) and (d)). The reason for that lies in the simple nature of the model. Considering the assumptions mentioned in Section 2.2, not only the kinetic constants are coverage independent but also the catalytic adsorption sites are equivalent and have the same "stability" (quantified by the binding energy). Additionally, our model does not include support interaction.

It is found that the rate of DRM at low CO_2 partial pressure ($\leq$ 10 kPa) [25] is directly depended on the value of the CO_2 partial pressure. This suggests that CO_2 adsorption is among the kinetically relevant reaction steps for the given condition. Moreover, the catalysts that are employed in the experiment have a catalyst support. Typically, these are modified metal oxides like MgO or Al_2O_3. These oxides positively affect the basicity of the catalyst and hence improve CO_2 interaction with the catalyst surface. Since our model works within the constraints of the model assumptions (See section 2.2) and does not include support interactions, it underestimates the reactant conversion and, hence, overestimates their concentration at the exit for temperatures where the reaction is kinetically controlled.

However, at higher temperatures, the reaction slowly proceeds towards thermodynamic equilibrium and the reactant conversions are more thermodynamically controlled. Therefore, given the exit concentration values at high temperatures, we can explain why this region is in good agreement with experiments.

Table S5. Forward reaction rates of elementary steps on Ni (111) and B-doped Ni surface at reaction conditions adapted from section 3.2.1

Elementary reactions	Forward Reaction Rate ($mol \cdot g_{cat}^{-1} \cdot h^{-1}$)	
	Ni (111)	B-doped Ni
R1: $CH_4^* \rightarrow CH_3^* + H^*$	1.603027027	1074.091219
R2: $CH_3^* \rightarrow CH_2^* + H^*$	56.80512603	715.7788407
R3: $CH_2^* \rightarrow CH^* + H^*$	7918.634495	845.403961
R4: $CH^* \rightarrow C^* + H^*$	32.41876188	59.69663392
R5: $CO_2^* \rightarrow CO^* + O^*$	336.0022487	176.9330479
R6: $CO_2^* + H^* \rightarrow COOH^*$	0.050513086	0.038640049
R7: $CO_2^* + H^* \rightarrow HCOO^*$	11.54853185	1036.222628
R8: $COOH^* \rightarrow CO^* + OH^*$	589.9211959	46.73137006
R9: $HCOO^* \rightarrow HCO^* + O^*$	0.006514089	0.001106794
R10: $HCO^* \rightarrow CO^* + H^*$	1339.217144	3948.375492
R11: $COOH^* + H^* \rightarrow HCOOH^*$	0.003804539	0.021280521
R12: $HCOO^* + H^* \rightarrow HCOOH^*$	0.102806242	2.110301158

R13: HCOOH*→HCO*+OH*	0.01049494	0.006930301
R14: CH_3OH*→CH_2OH*+H*	7.00431E-08	0.000150214
R15: CH_2OH*→CHOH*+H*	3.6391E-05	0.121235684
R16: CHOH*→COH*+H*	0.119111159	0.13852291
R17: COH*→CO*+H*	0.270604786	0.107000273
R18: CH_3*+OH* →CH_3OH*	7.2561E-08	2.08153E-05
R19: CH_2*+OH*→CH_2OH*	0.000237822	2.55077424
R20: CH*+OH*→ CHOH*	0.049621745	0.042415326
R21: C*+OH*→COH*	0.006960343	0.006492443
R22: CH_3O*→CH_2O*+H*	0.002476634	0.026659696
R23: CH2O*→CHO*+H*	0.103005432	0.497703202
R24: CH_3*+O* →CH_3O*	0.002153093	0.01773012
R25: CH_2*+O*→CH_2O*	0.014518412	0.173170659
R26: CH*+O*→ CHO*	1.282131382	0.002020685
R27: C*+O*→CO*	0.020101874	0.000100607
R28: CH_3OH*+*→ CH_3O*+H*	2.12305E-05	0.003641637
R29: CH_2OH*+*→ CH_2O*+H*	4.65783E-05	0.006627168
R30: CHOH*+*→ HCO*+H*	0.001274997	0.058060651
R31: O*+H*→OH*	647.2158212	20.71594681
R32: OH*+H*→H_2O*	3.172545558	56.29392543
R33: H*+H*→H_2	3944.6944	407.1332247
R34: OH*+OH*→H_2O*+O*	24.568704	2946.185567
R35: CO_2*+C*→2CO*	1.71612E-06	0.000154338
R36: CO_2→CO_2*	21.04971811	293.2282616
R37: CO*→CO	263633.4331	1012873.897
R38: H_2O* →H_2O + *	459062.2087	253156.7925

S5. Reaction mechanism analysis

Once the RDS is identified, the dominant reaction pathway is formulated for product formation, i.e. the pathway whose rate limiting step is same as the RDS identified for the overall reaction. The approach is to first compare reaction rates of every elementary reaction steps with the rate of RDS and exclude the steps with rates lower than the RDS. Then compare the rates of selected steps to identify the fastest pathway form gaseous reactants (CH_4(g), CO_2(g)) to RDS's reactant intermediates and RDS's product intermediates to gaseous products (H_2(g), CO(g)). Side reaction steps of RWGS, except H_2 formation/dissociation ($H^*+H^*=H_2$), are not included in the selected reaction steps as they do not lead to desired product formation.

The fastest pathway is identified step by step in the following manner. First the necessary reaction steps, i.e. adsorption of reactants, RDS and desorption of products are listed. Then the reactant dissociation steps are included in this pathway. If there are more than one reaction step for reactant dissociation, only the step with highest rate of dissociation (i.e. fastest dissociation step) is included as it is contributing the most towards reactant dissociation. From the dissociation product, again the fastest reaction step towards RDS's reactant formation is added. Similarly, the fastest step leading to product formation from the RDS's product is incorporated which is followed by the desorption step.

S6. Sensitivity analysis for DRM on Ni (111) at varying reaction condition

The results of the simulations performed to identify the different kinetically relevant steps on Ni (111) over a range of reaction conditions are presented here.

Table S6 enlists these different reactions conditions or cases.

Table S6. Different reaction conditions for sensitivity analysis. Pressure and inlet feed composition were varied over four cases and the sensitivity analysis was performed for each case at three reaction temperatures, i.e. 873 K, 973 K, and 1073 K.

	Pressure	Inlet feed composition (Volume fraction)
Case 1	10 bar	CO_2: 50%, CH_4: 50%
Case 2	10 bar	CO_2: 2%, CH_4: 2%, N_2: 96%
Case 3	1 bar	CO_2: 50%, CH_4: 50%
Case 4	1 bar	CO_2: 2%, CH_4: 2%, N_2: 96%

Case 1: Pressure 10 bar, CO_2: 50%, CH_4: 50%

Figures S4, S5 and S6 report the relative sensitivity coefficients for the above case at temperatures 873 K, 973 K and 1073 K respectively.

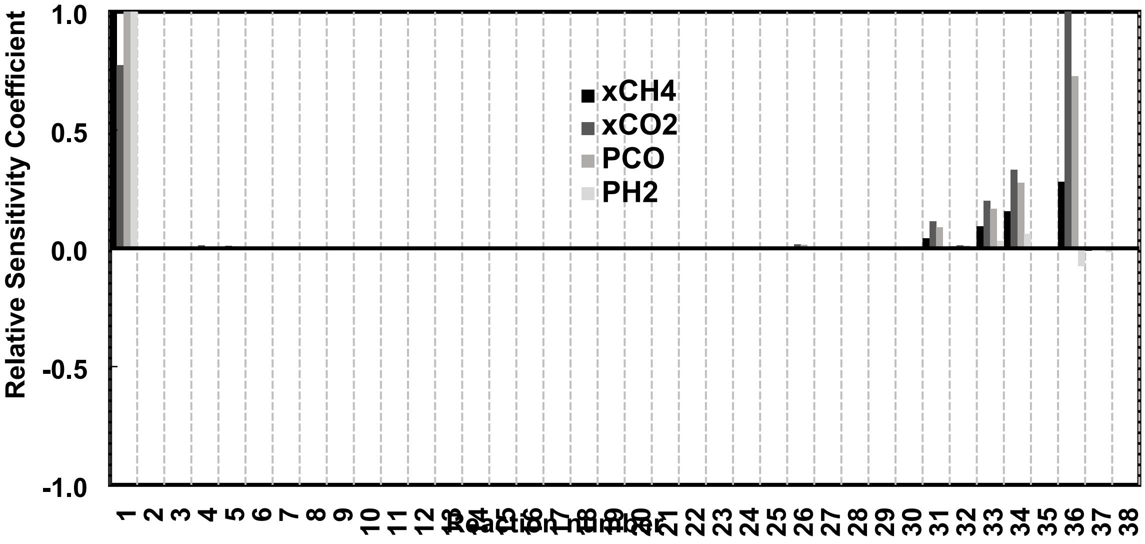

Figure S4. Sensitivity analysis of DRM reaction steps over Ni (111) surfaces at space time value of 0.01 $g_{cat}\cdot h\cdot mol^{-1}$ at 873 K for Case 1 (Pressure 10 bar, CO_2: 50%, CH_4: 50%) reaction conditions.

At 873 K (see Figure S4), adsorption of reactants are the most sensitive steps and their conversion is completely dependent on their respective rates of adsorption (R1 and R36). However, the amount of syngas produced is more sensitive towards the elementary step of the dissociative adsorption of CH_4 (R1).

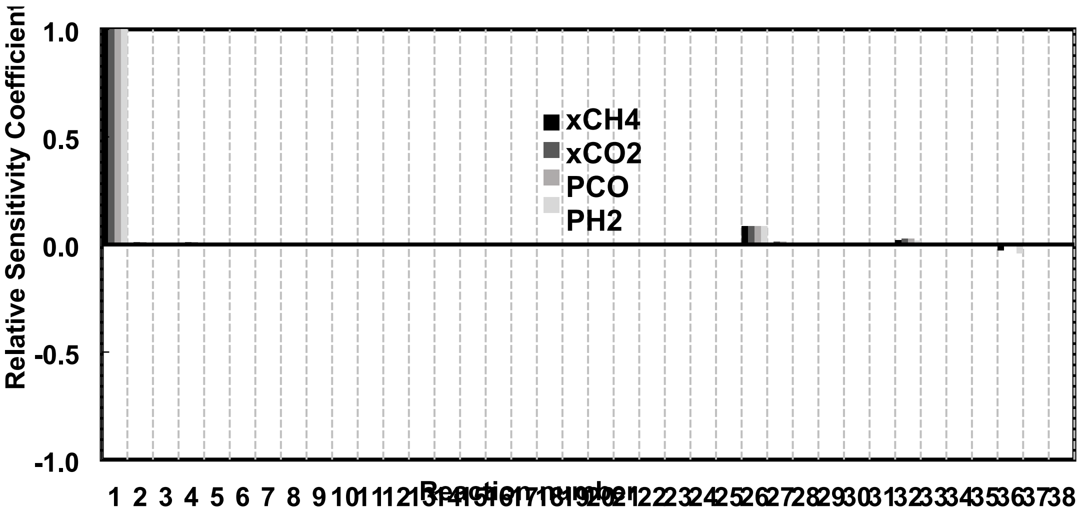

Figure S5. Sensitivity analysis of DRM reaction steps over Ni (111) surfaces at space time value of 0.01 g_{cat}·h·mol^{-1} at 973 K for Case 1 (Pressure 10 bar, CO_2: 50%, CH_4: 50%) reaction conditions.

As the reaction temperature increases to 973 K, the model responses become more sensitive towards R1 but are no longer sensitive to R36. At 1073 K, R1 still remains the most sensitive reaction step, however CH* oxidation (R26) is now among the kinetically relevant steps and is half as sensitive as R1 towards the model responses.

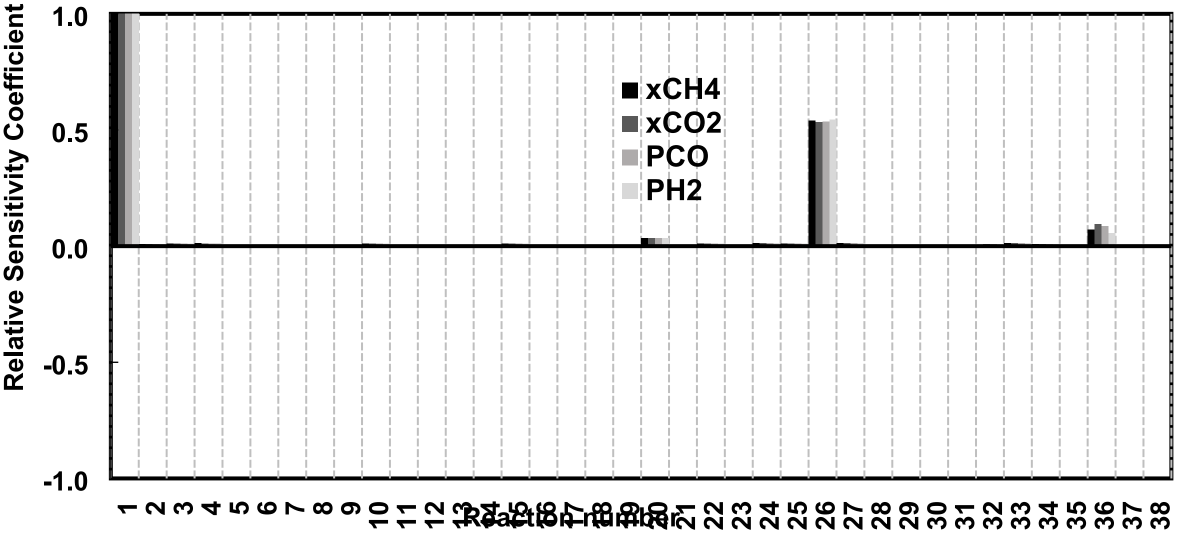

Figure S6. Sensitivity analysis of DRM reaction steps over Ni (111) surfaces at space time value of 0.01 g_{cat}·h·mol^{-1} at 1073 K for Case 1 (Pressure 10 bar, CO_2: 50%, CH_4: 50%) reaction condition

From the sensitivity analysis, we can conclude that CH_4 dissociation is the most sensitive elementary step throughout the temperature range with the CO_2 adsorption (R36) and CH* oxidation (R26) being relevant at lower (873 K) and higher (1073 K) temperatures respectively. A partial equilibrium analysis was further performed to identify the RDS for the given the reaction conditions.

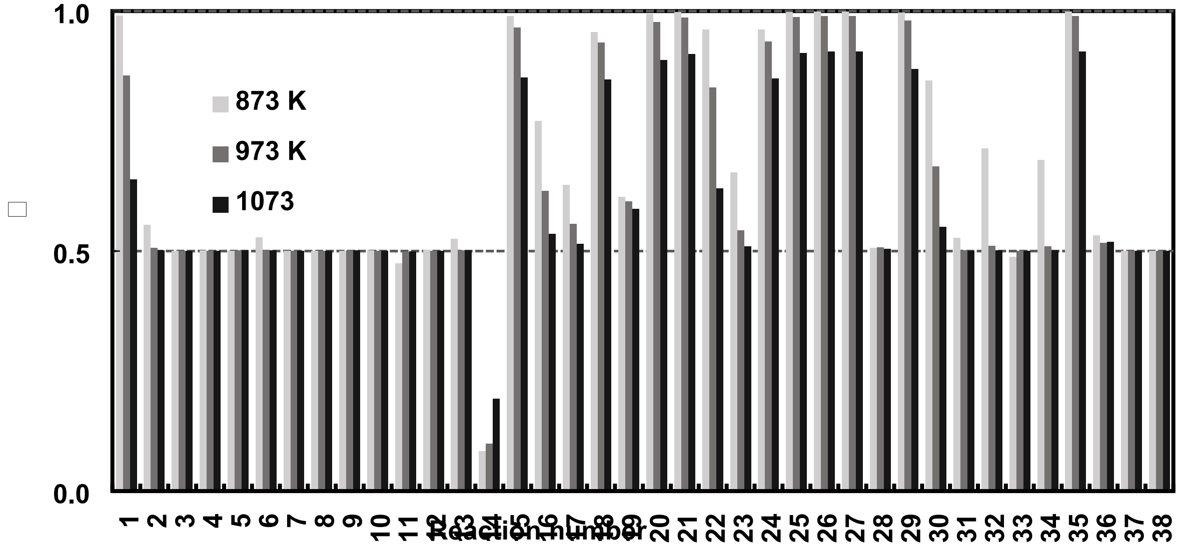

Figure S7. Partial equilibrium coefficient φ of DRM reaction steps over Ni (111) surfaces at space time value of 0.01 $g_{cat}\cdot h\cdot mol^{-1}$ at varying temperature for Case 1 (Pressure 10 bar, CO_2: 50%, CH_4: 50%) reaction condition

From Figure S7, we can observe that all three relevant elementary steps obtained from sensitivity analysis (i.e. R1, R26 and R36) are not in quasi equilibrium and are hence candidates for RDS. However, R1 is the most sensitive step given the temperature range and hence contributes the most to the overall reaction rate. Therefore, CH_4 dissociative adsorption (R1) is the RDS for this case.

Case 2: Pressure 10 bar, CO_2: 2%, CH_4: 2%, N_2: 96%

This section reports the relative sensitivity coefficients (at reaction temperatures of 873 K, 973 K and 1073 K) for the case where the inlet feed consists of a major fraction of inert gas.

With the inert gas having a volume fraction of 96%, the partial pressure of CH_4 and CO_2 reduces to 20 kPa each. The sensitivity analysis at 873 K shows that the dissociative adsorption of CH_4 (R1) and adsorption of CO_2 (R2) are the most sensitive steps and the reactant conversions are completely dependent on their respective rates of adsorption (R1 and R36). Although unlike previously observed for Case 1, 873 K, (Figure S4) the product formation is relatively more sensitive to the CO_2 adsoption step.

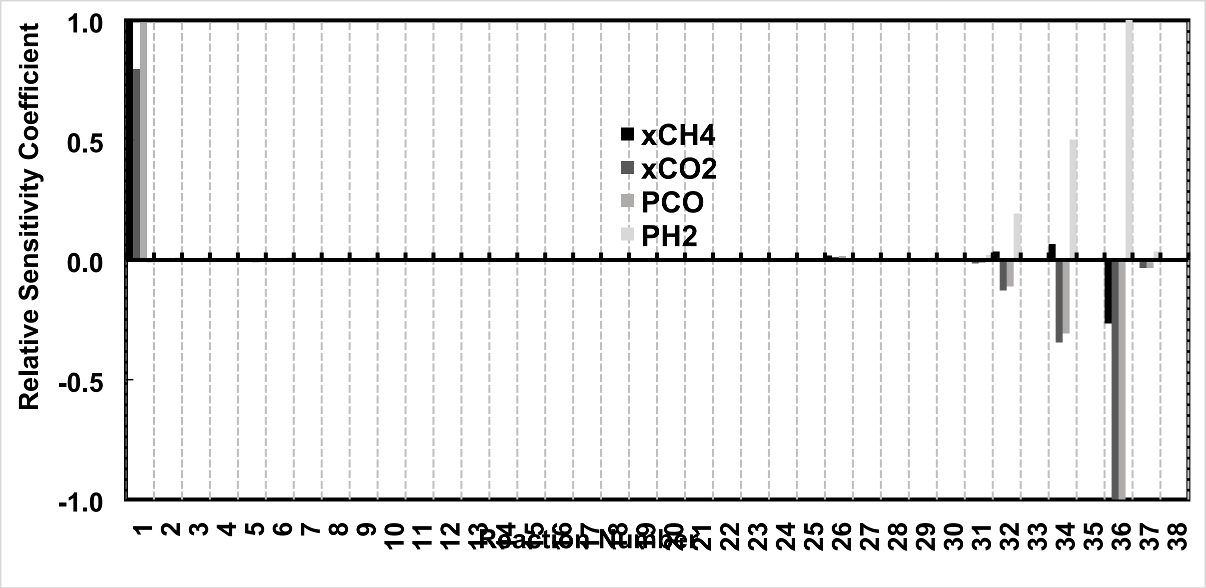

Figure S8. Sensitivity analysis of DRM reaction steps over Ni (111) surfaces at space time value of 0.01 $g_{cat}\cdot h\cdot mol^{-1}$ at 873 K for Case 2 (Pressure 10 bar, CO_2: 2%, CH_4: 2%, N_2: 96%) reaction conditions.

This, however, changes as temperature increases to 973 K (see Figure S9). CH_4 dissociation becomes the most sensitive step and the other relavant steps are similar to those in Case 1 at 1073 K (see Figure S6).

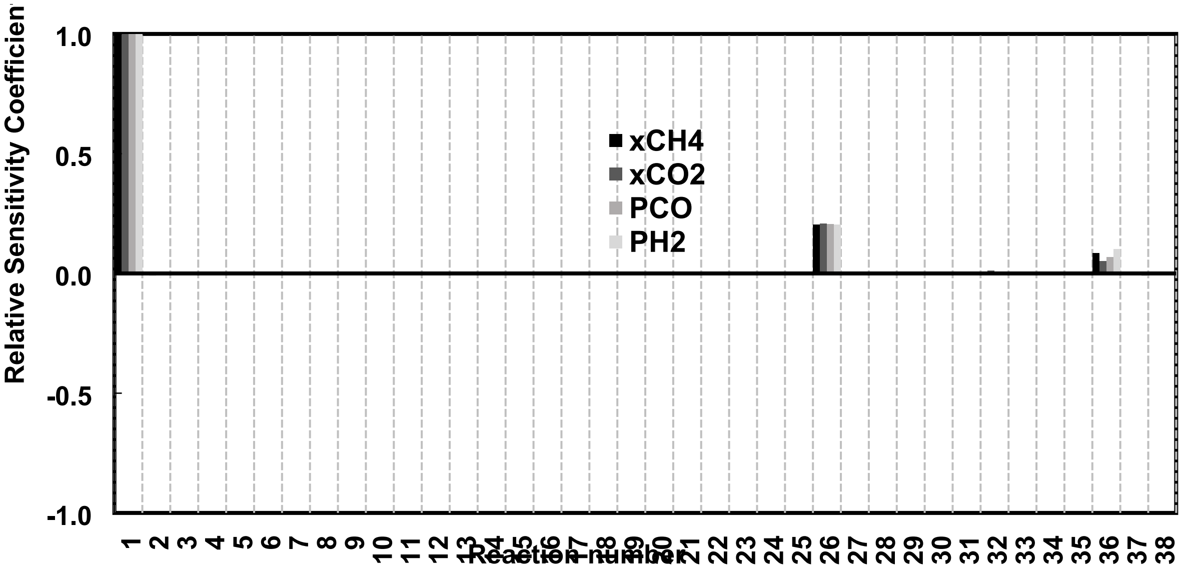

Figure S9. Sensitivity analysis of DRM reaction steps over Ni (111) surfaces at space time value of 0.01 $g_{cat}\cdot h\cdot mol^{-1}$ at 973 K for Case 2 (Pressure 10 bar, CO_2: 2%, CH_4: 2%, N_2: 96%) reaction condition

At 1073 K, the overall reaction approaches equillibrium (see Figure S10) and the model responses are sensitive to more elementary steps, with the most sensitive reaction being CH* oxidation (R26) followed by adsorption of reactants (R1 and R36). A further partial equillibrium analysis was performed to identify the RDS for different reaction temperatures.

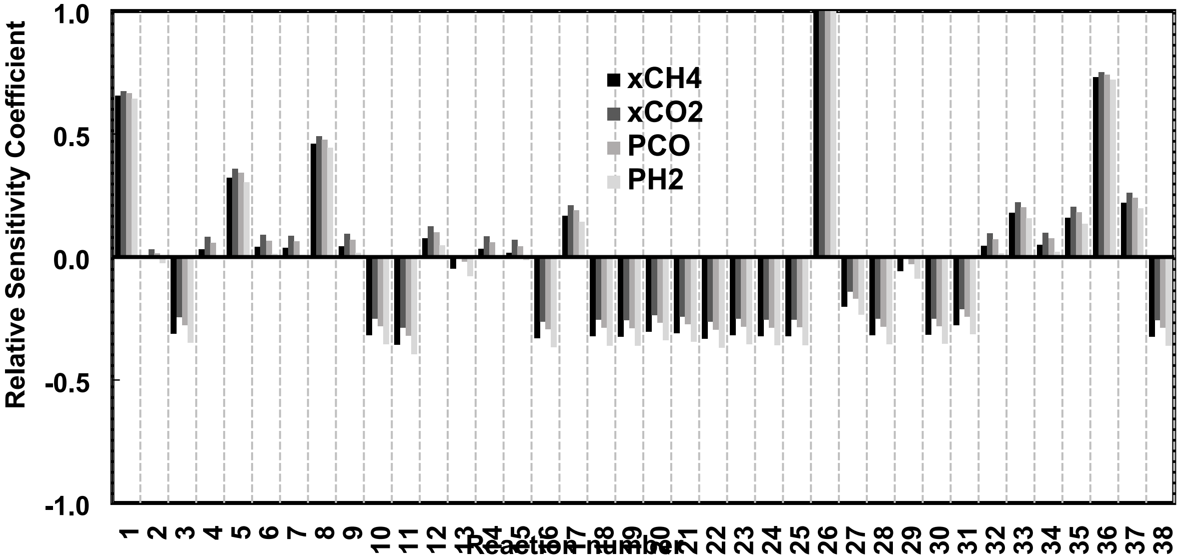

Figure S10. Sensitivity analysis of DRM reaction steps over Ni (111) surfaces at space time value of 0.01 (g_{cat}·h·mol^{-1}) at 1073 K for Case 2 (Pressure 10 bar, CO_2: 2%, CH_4: 2%, N_2: 96%) reaction conditions.

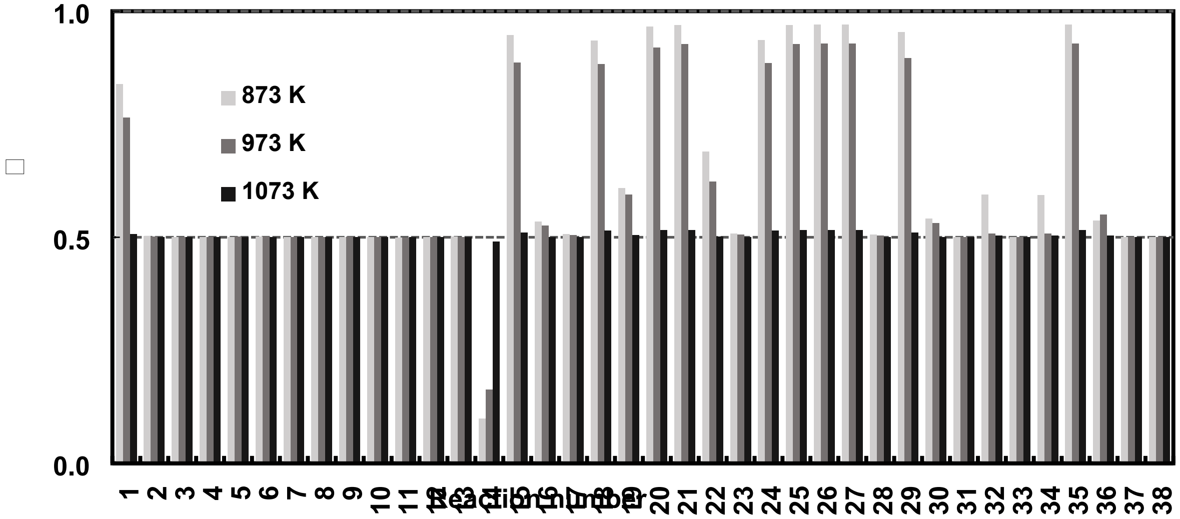

Figure S11. Partial equilibrium coefficient φ of DRM reaction steps over Ni (111) surfaces at space time value of 0.01 g_{cat}·h·mol^{-1} at varying temperature for Case 2 (Pressure 10 bar, CO_2: 2%, CH_4: 2%, N_2: 96%) reaction conditions.

Figure S11 shows that all three relevant elementary steps obtained from sensitivity analysis (i.e. R1, R26 and R36) are not in quasi equilibrium except at 1073K. At 873 K, both reactants conversions are sensitive to their respective adsorption reactions, hence based on the results of sensitivity analysis and partial equilibrium analysis we can conclude that the overall rate for DRM, at 873 K and given reaction conditions, should depend on the rate adsorption of CH_4 and CO_2. However, if we were to choose a rate determining step, it should be decided directly based on the computed forward rate values. At the given reaction conditions, forward reaction rates of R1 and R36 are 0.017 and 0.116 in $mol{\cdot}h^{-1}{\cdot}g_{cat}^{-1}$ respectively, hence R1 is the RDS. For reaction temperatures 973 K and 1073 K, the rate determining steps are undoubtedly R1 and R26 respectively.

Case 3: Pressure 1 bar, CO_2: 50%, CH_4: 50% and Case 4: Pressure 1 bar, CO_2: 2%, CH_4: 2%, N_2: 96%

As observed previously (Figure S4 and S8), the reactant adsorption steps (R1 and R36) are found to be the most sensitive steps. However, unlike the previous cases, the reactant adsorption steps remain the most sensitive steps throughout the temperature range (Figure S12-S17). The reactant conversions depend mostly on their respective rates of adsorption (R1 and R36) and the H_2 and CO exit pressures are more sensitive to R1 at lower temperatures (see Figure S12 and S15). But, as the temperature increases, the CO exit pressure becomes more sensitive to R36 (see Figure S14 and S17).

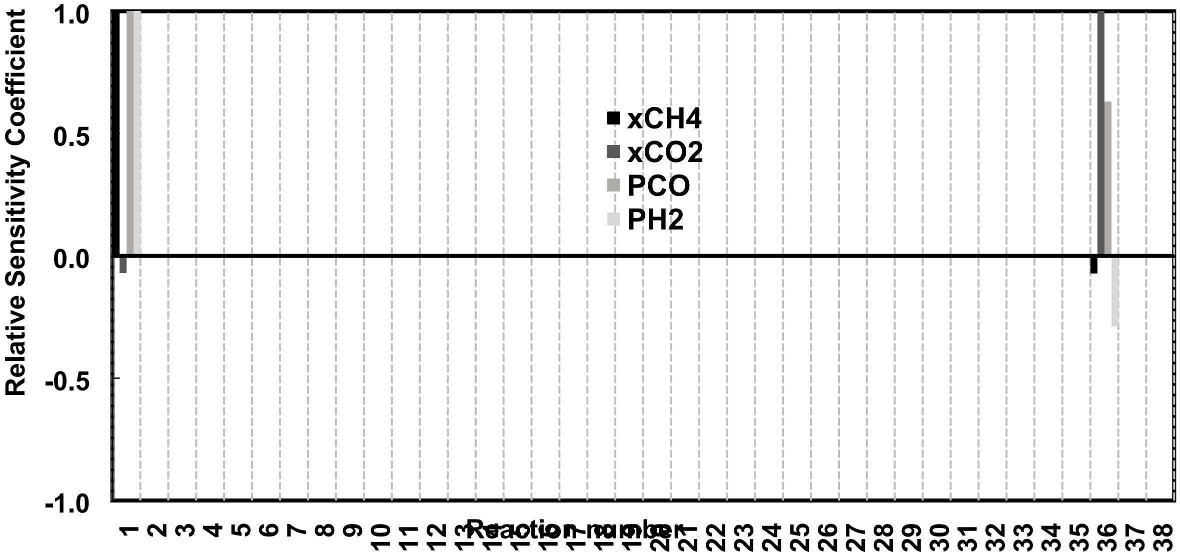

Figure S12. Sensitivity analysis of DRM reaction steps over Ni (111) surfaces at space time value of 0.01 $g_{cat}{\cdot}h{\cdot}mol^{-1}$ at 873 K for Case 3 reaction conditions.

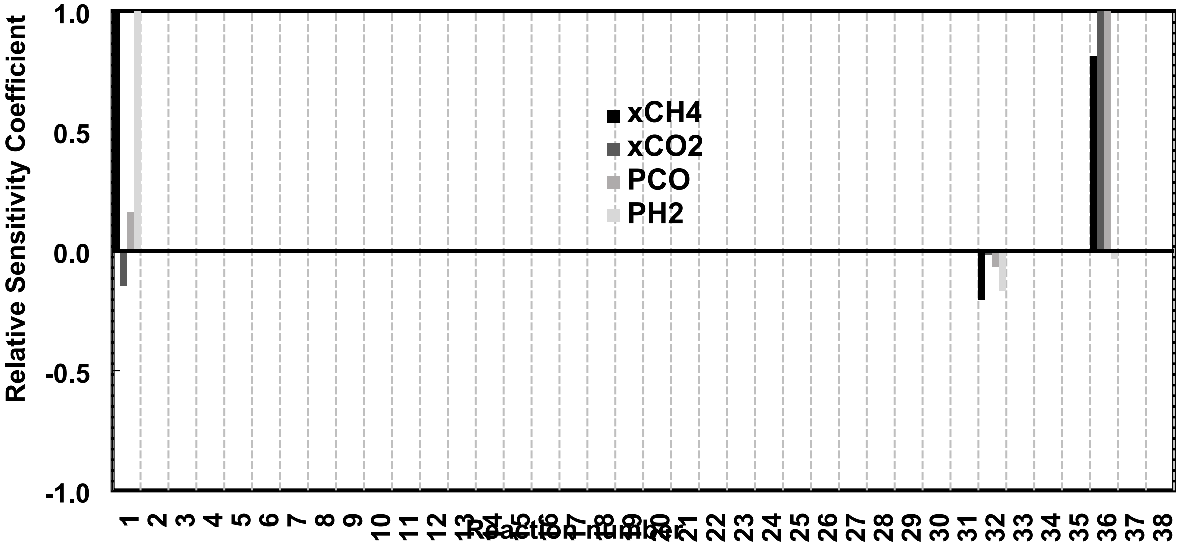

Figure S13. Sensitivity analysis of DRM reaction steps over Ni (111) surfaces at space time value of 0.01 g_{cat}·h·mol^{-1} at 973 K for Case 3 reaction conditions.

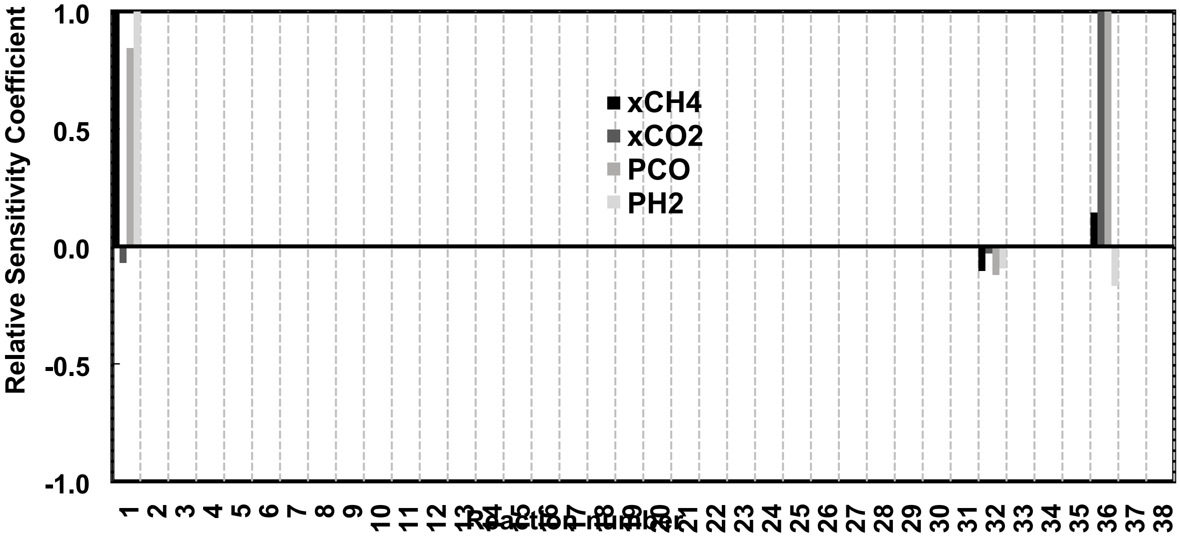

Figure S14. Sensitivity analysis of DRM reaction steps over Ni (111) surfaces at space time value of 0.01 g_{cat}·h·mol^{-1} at 1073 K for Case 3 reaction conditions.

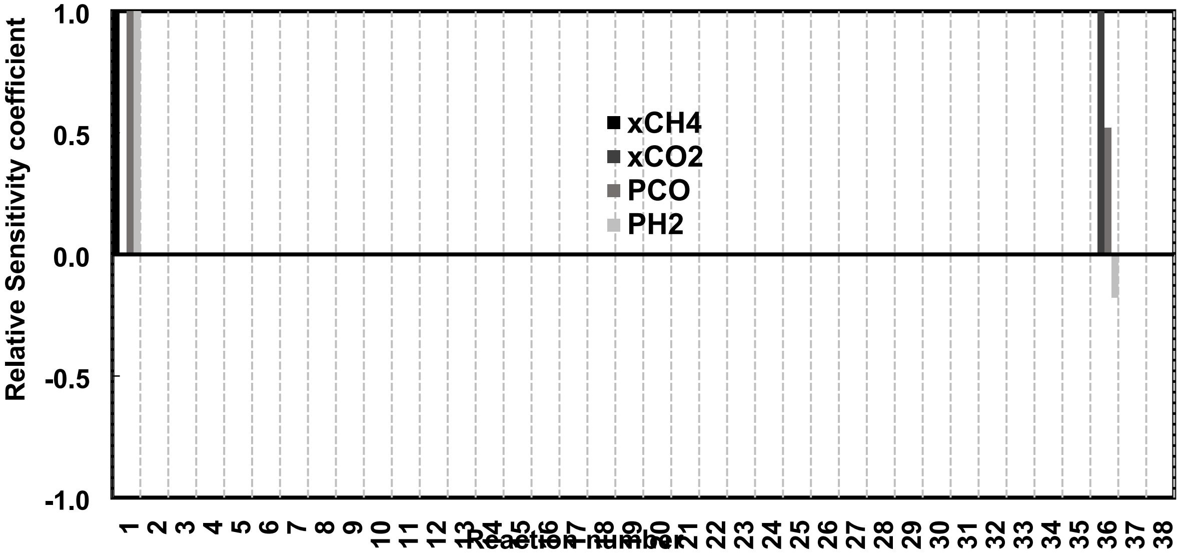

Figure S15. Sensitivity analysis of DRM reaction steps over Ni (111) surfaces at space time value of 0.01 $g_{cat}\cdot h\cdot mol^{-1}$ at 873 K for Case 4 reaction conditions.

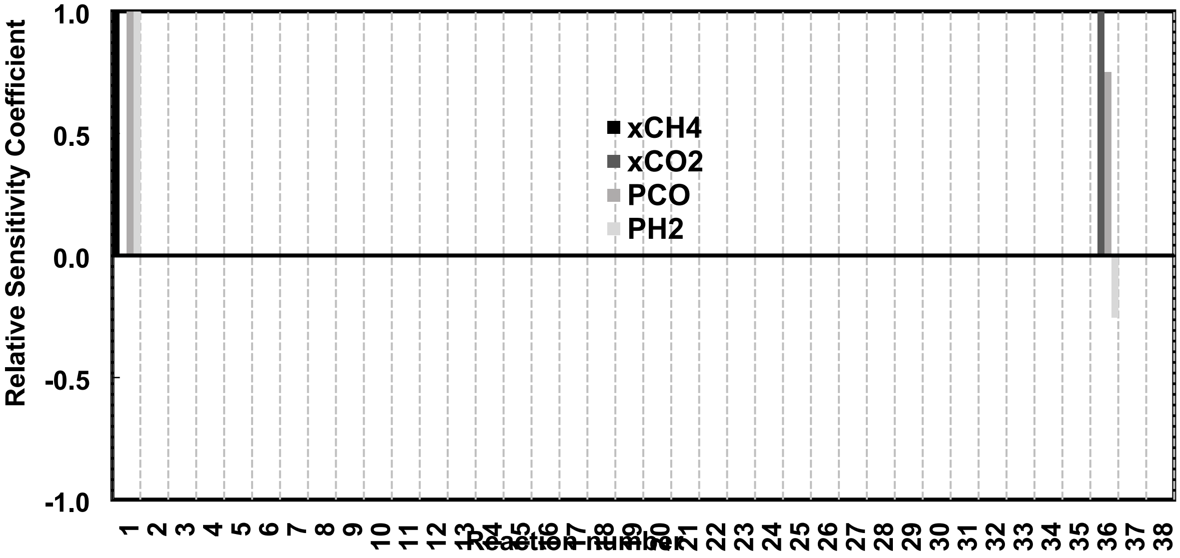

Figure S16. Sensitivity analysis of DRM reaction steps over Ni (111) surfaces at space time value of 0.01 $g_{cat}\cdot h\cdot mol^{-1}$ at 973 K for Case 4 reaction conditions.

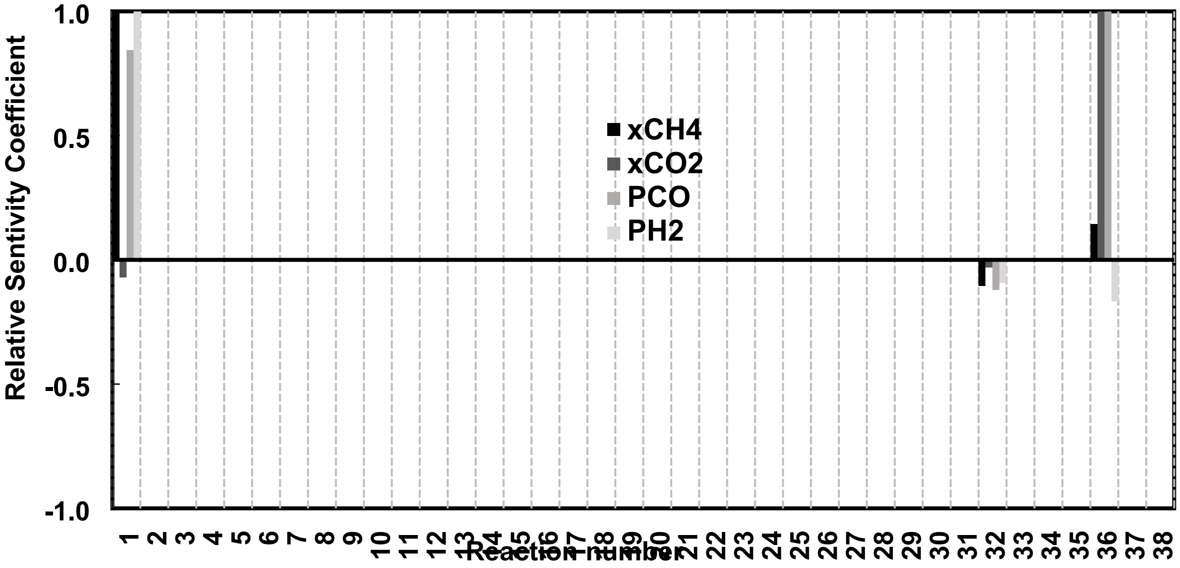

Figure S17. Sensitivity analysis of DRM reaction steps over Ni (111) surfaces at space time value of 0.01 (g_{cat}·h·mol^{-1}) at 1073 K for Case 4 reaction conditions.

As observed from the sensitivity analysis (Figure S12-S17), the R1 and R36 are the most sensitive steps, and the overall rate of DRM must depend on these adsorption reaction steps. However, it is difficult to identify the RDS solely from the sensitivity analysis. Hence, the RDS for case 3 and 4 were directly decided based on the computed forward reaction rates of R1 and R36. The rates are given in Table S7.

Table S7. Computed forward reaction rates of R1 and R36 over Ni (111) at space time value of 0.01 g_{cat}·h·mol^{-1} for varying temperature for Case 3 and 4 reaction condition.

Temperature	Case 3		Case 4	
	R1 (mol·h^{-1}·g_{cat}^{-1})	R36 (mol·h^{-1}·g_{cat}^{-1})	R1 (mol·h^{-1}·g_{cat}^{-1})	R36 (mol·h^{-1}·g_{cat}^{-1})
873 K	0.612	1.136	0.045	0.046
973 K	3.526	3.605	0.218	0.223
1073 K	10.640	12.016	0.600	0.611

Based on the forward reaction rates reported in Table S7, we can conclude that R1 is RDS for cases 3 and 4 throughout the temperature range.

However, it should be noted that the difference in the forward rates of R1 and R36 are quite small for case 4. This is because as per the case 4 reaction conditions, the inert gas has a volume fraction of 96% and the partial pressure of CO_2 reduces to 2 kPa. Experiments have reported that at low CO_2 partial pressure (i.e. $\leq$ 10 kPa), varying this partial pressure strongly affects the overall rate of reaction[26,27], suggesting that the overall rate expression is sensitive to CO_2 adsoption (R36).

The sensitivity analysis (Figure S15-S17) and the forward reaction rates of R1 and R36 (Table S7) for case 4 show similar results. CO_2 adsorption (R36) is among the most sensitive steps of the DRM reaction and although CH_4 dissociative adsorption (R1) is the RDS, there is 6only a small diffrence in the forward rates of R1 and R36.

S7. Adsorption and transition state configurations on Ni (111) and NiB surfaces

(Blue balls represent Ni atoms, salmon balls represent B atoms, red balls represent oxygen atoms, white balls represent hydrogen atoms and grey balls represents carbon atoms)

Intermediate Structures on Ni (111)

1. CH_4

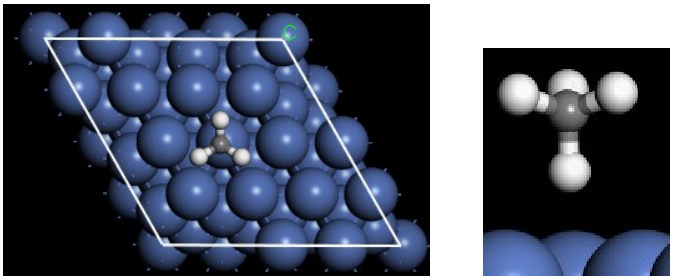

2. CH_3

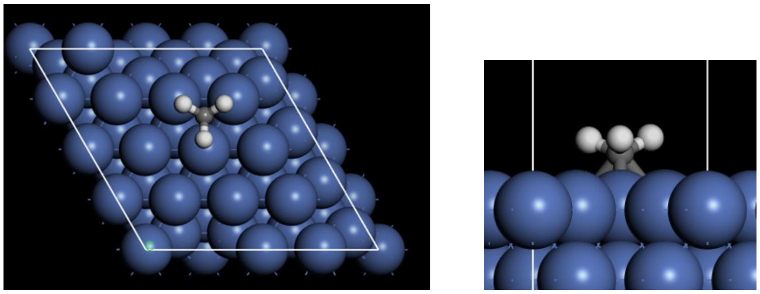

3. CH_2

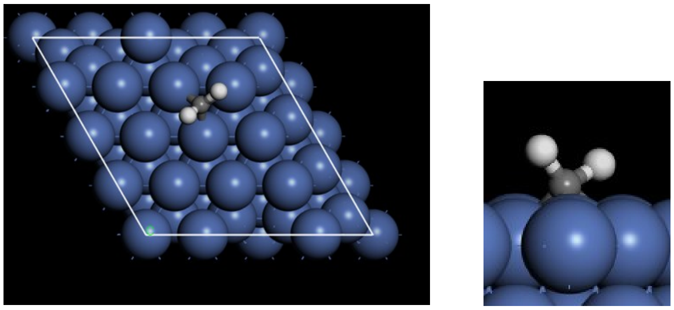

4. CH

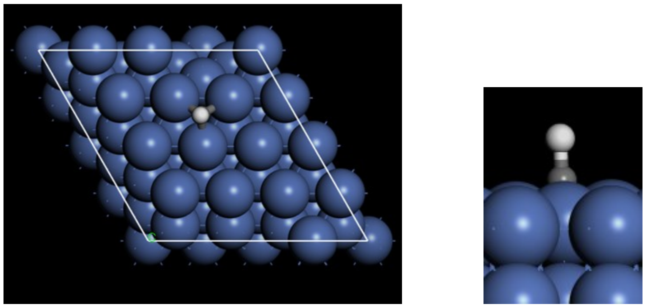

5. C

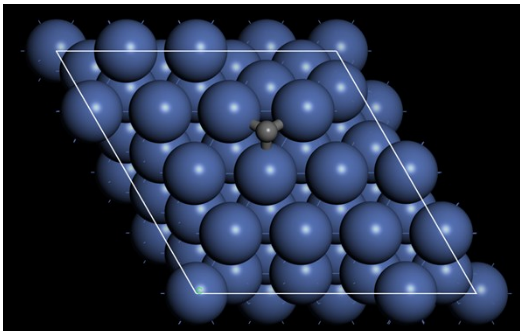

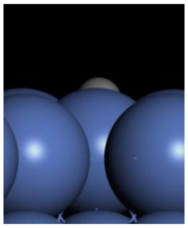

6. CO_2

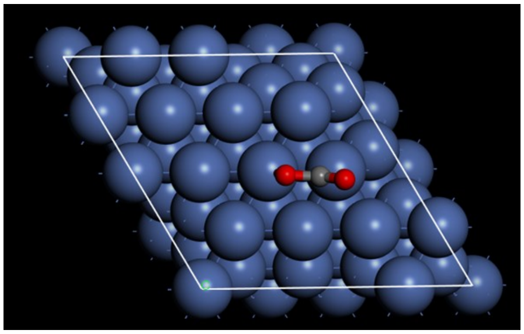

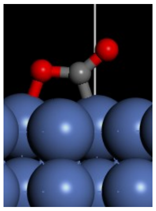

7. CO

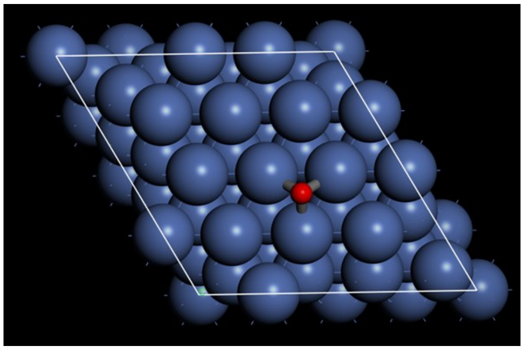

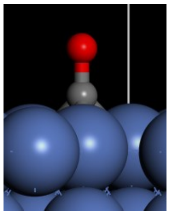

8. COOH

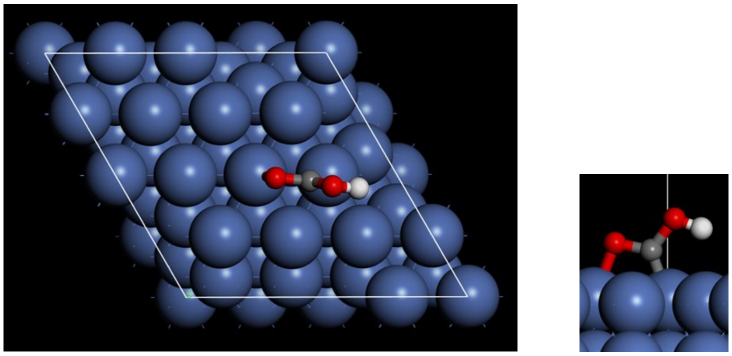

9. HCOO

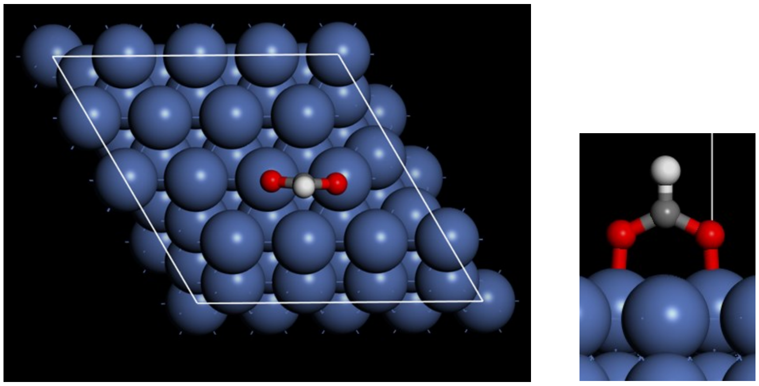

10. HCO

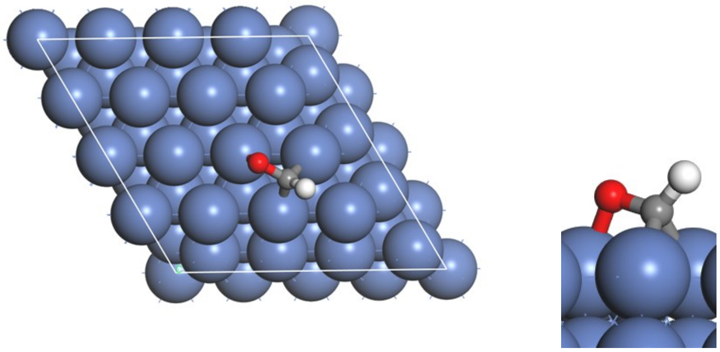

11. HCOOH

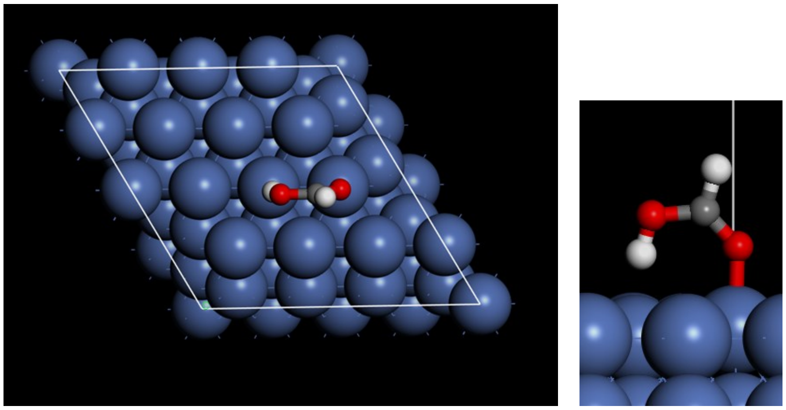

12. CH_3OH

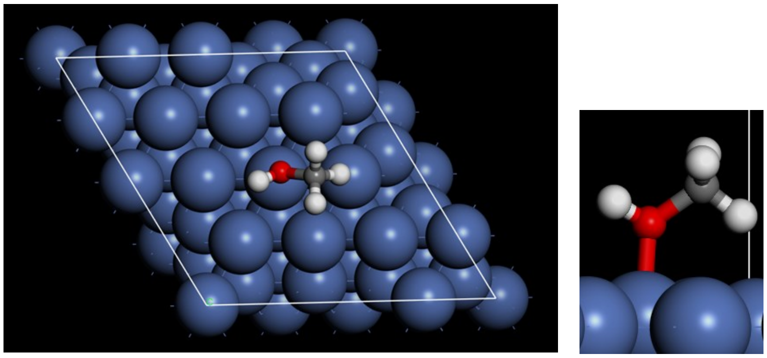

13. CH_2OH

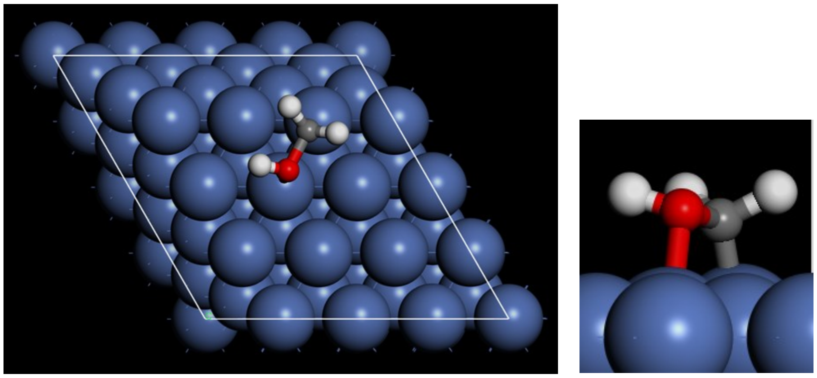

14. CHOH

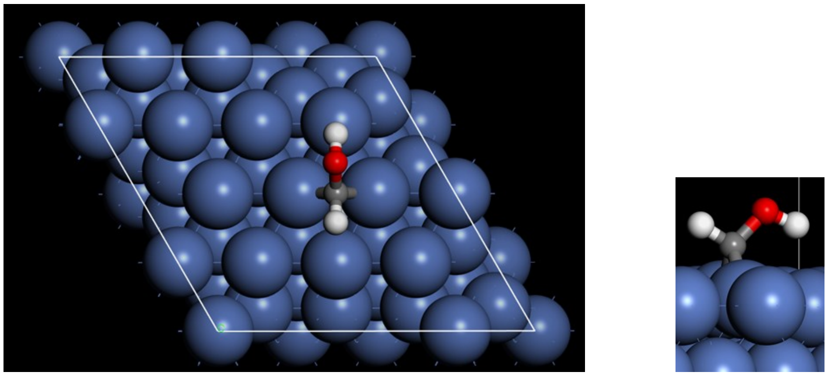

15. COH

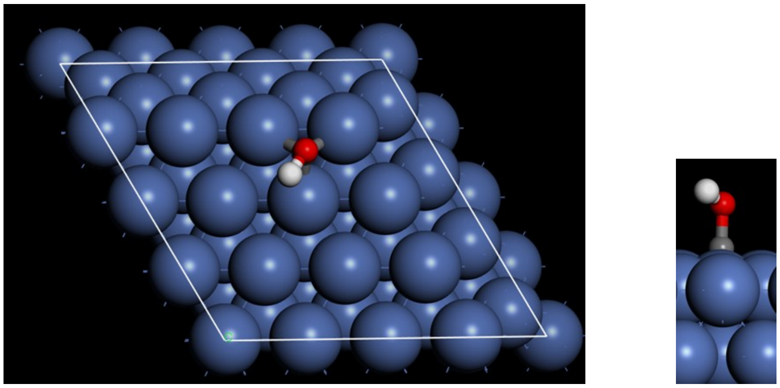

16. CH_3O

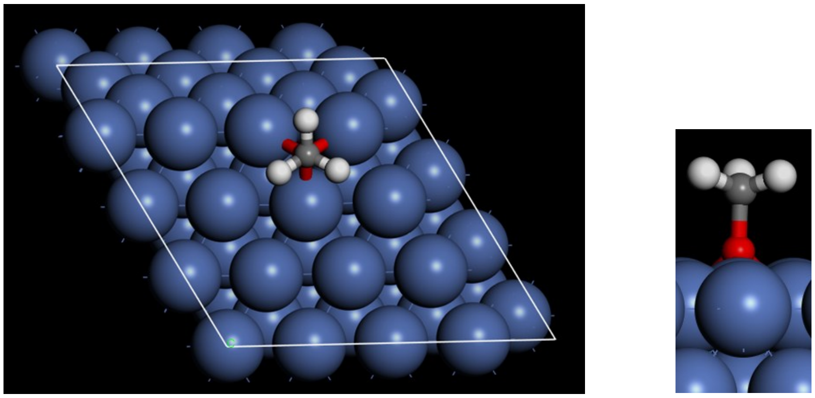

17. CH_2O

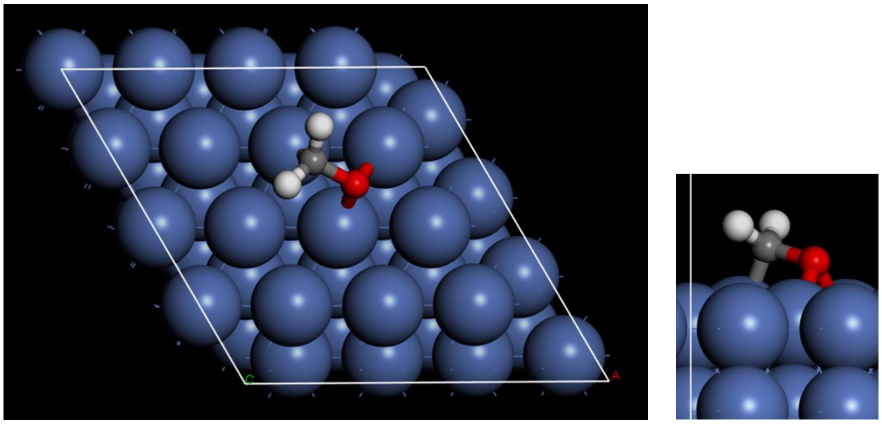

18. H_2O

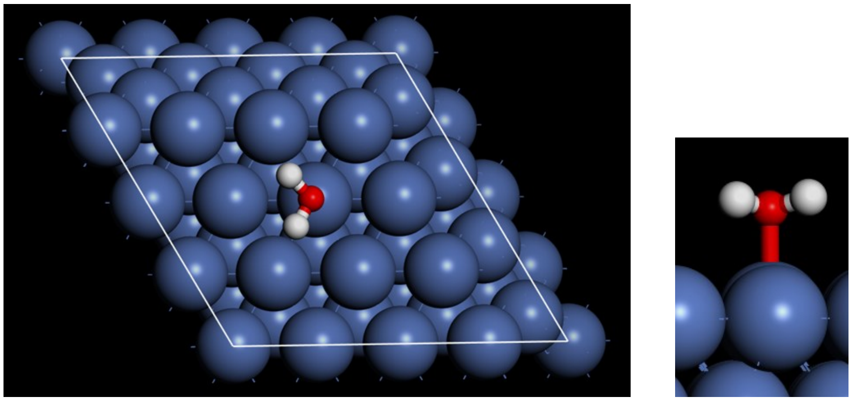

19. O

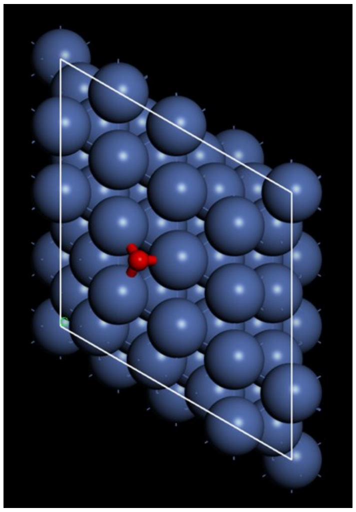

20. H

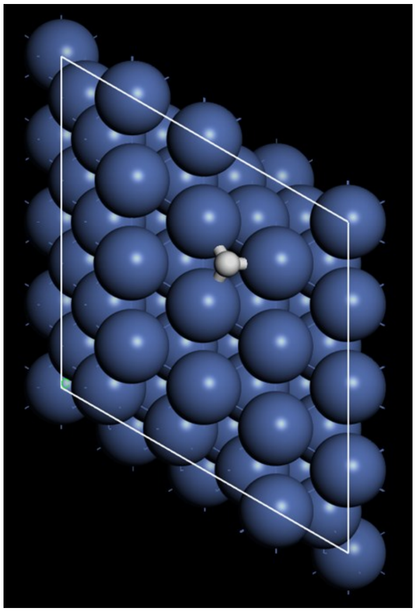

21. OH

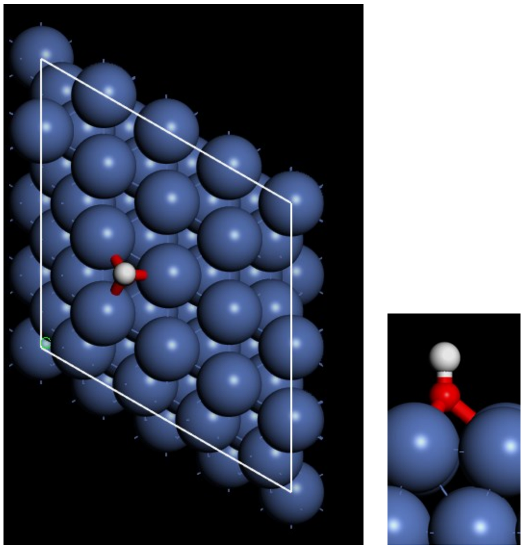

Ni (111)----TS structures

1. $CH_4 \rightarrow CH_3* + H*$

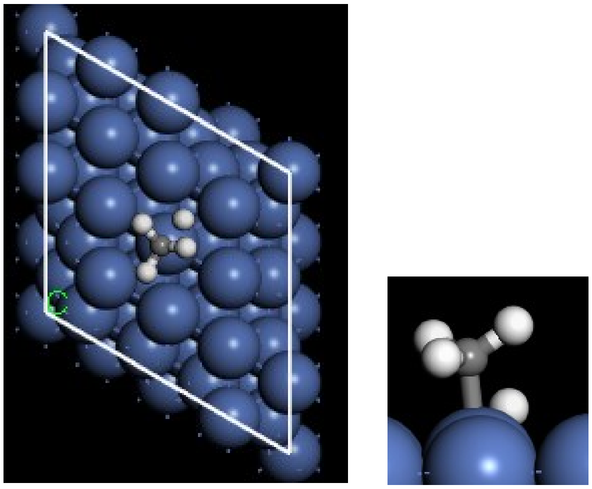

2. $CH_3* \rightarrow CH_2* + H*$

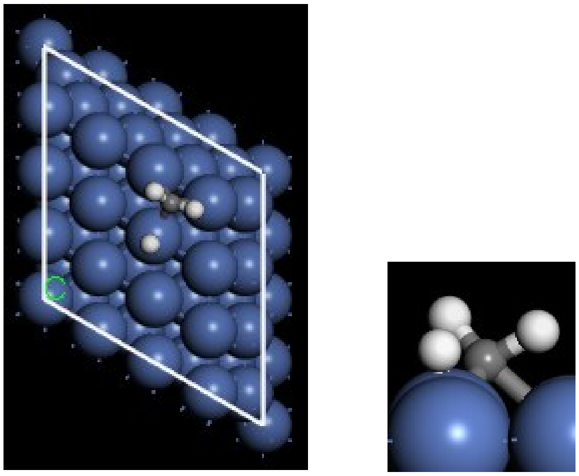

3. $CH_2* \rightarrow CH* + H*$

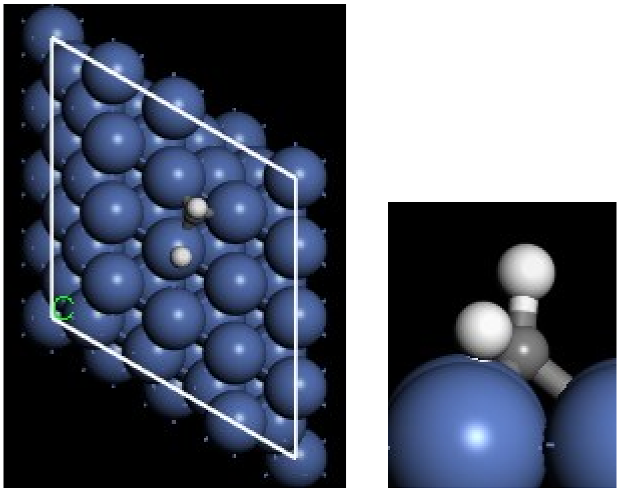

4. $CH^* \rightarrow C^* + H^*$

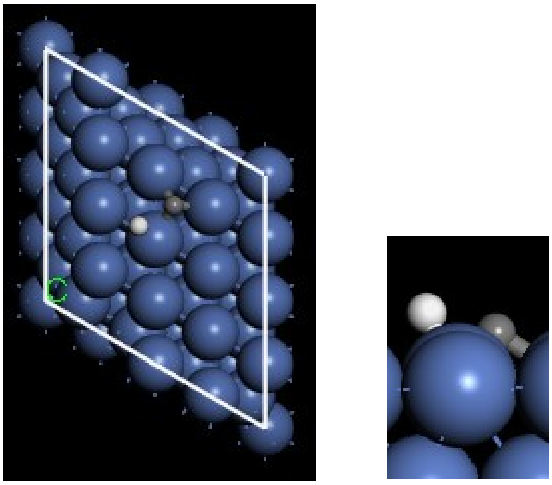

5. $CO_2^* \rightarrow CO^* + O^*$

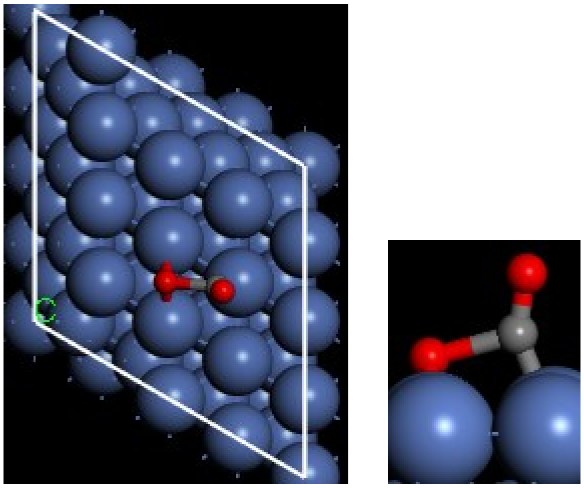

6. $CO_2^* + H^* \rightarrow COOH^*$

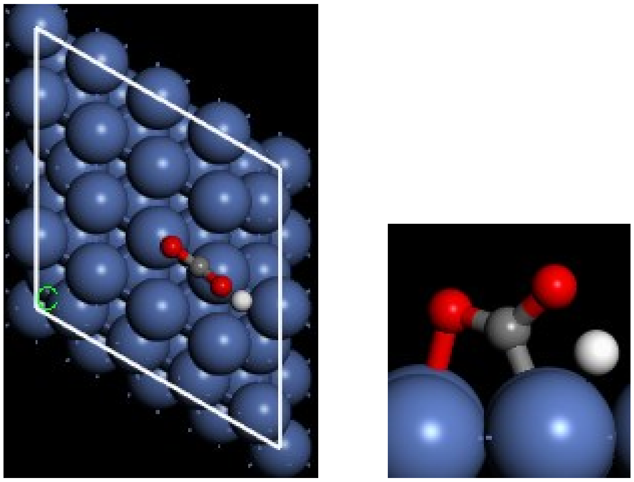

7. $CO_2^* + H^* \rightarrow HCOO^*$

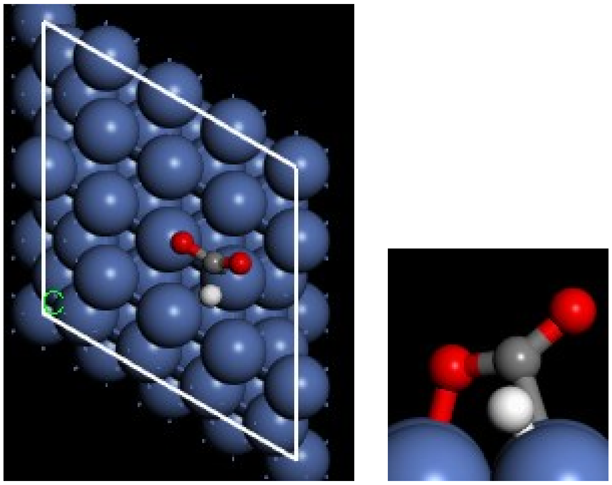

8. $COOH^* \rightarrow CO^* + OH^*$

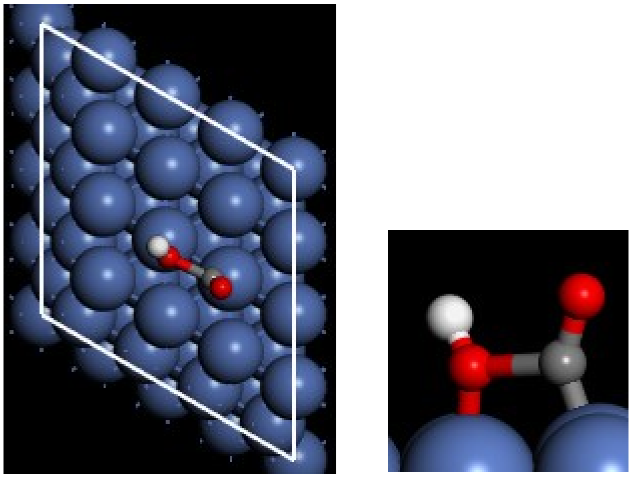

9. $HCOO^* \rightarrow HCO^* + O^*$

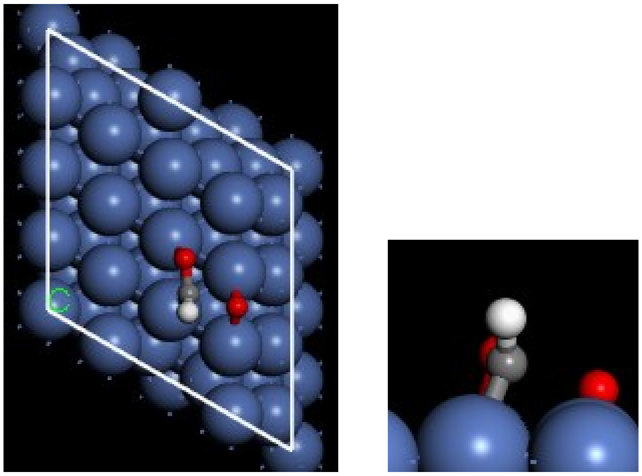

10. $HCO^* \rightarrow CO^* + H^*$

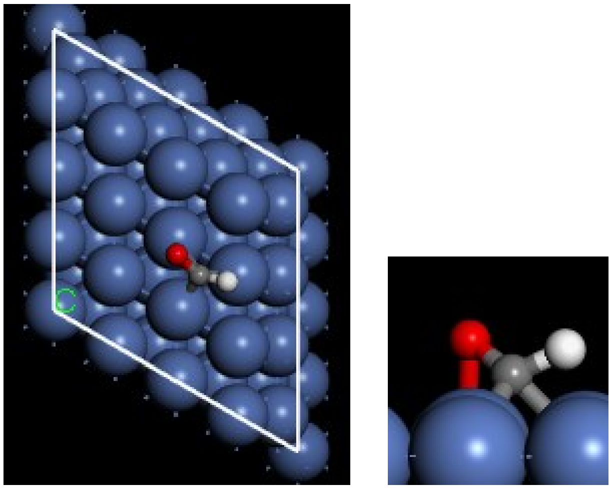

11. $COOH^* + H^* \rightarrow HCOOH^*$

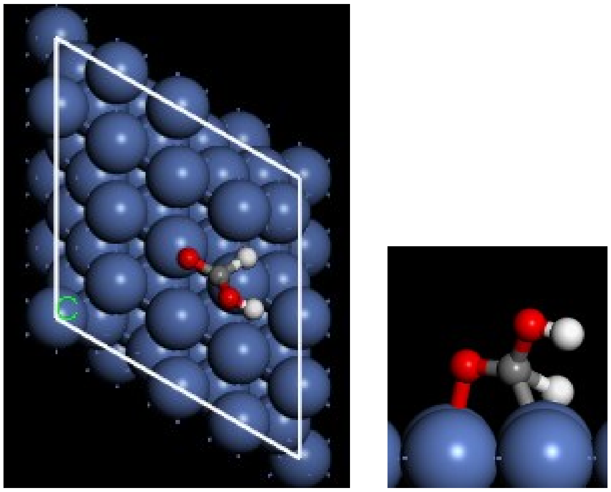

12. $HCOO^* + H^* \rightarrow HCOOH$

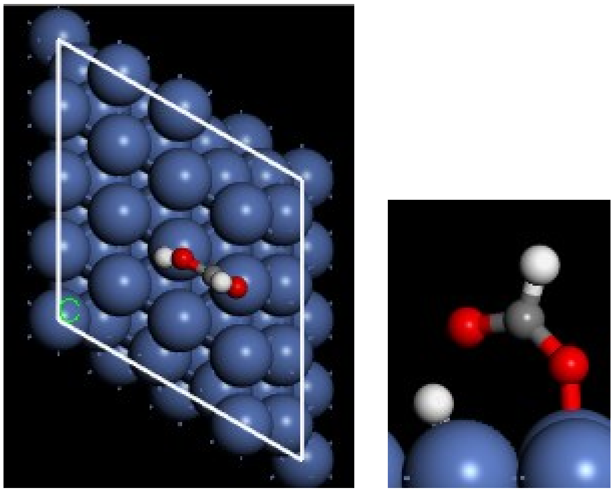

13. $HCOOH^* \rightarrow HCO^* + OH^*$

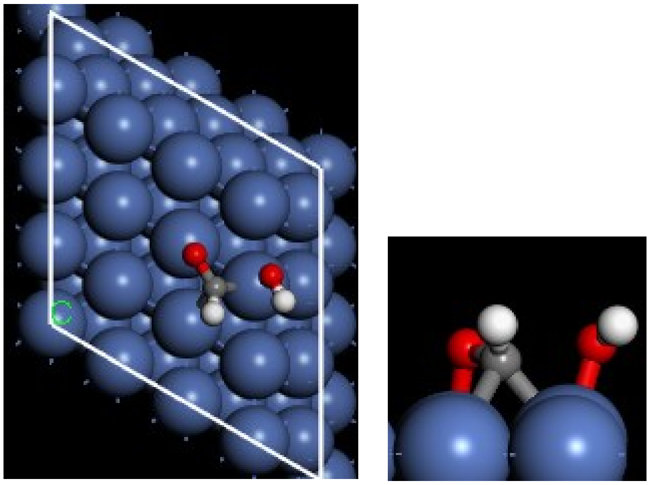

14. $CH_3OH^* \rightarrow CH_2OH^* + H^*$

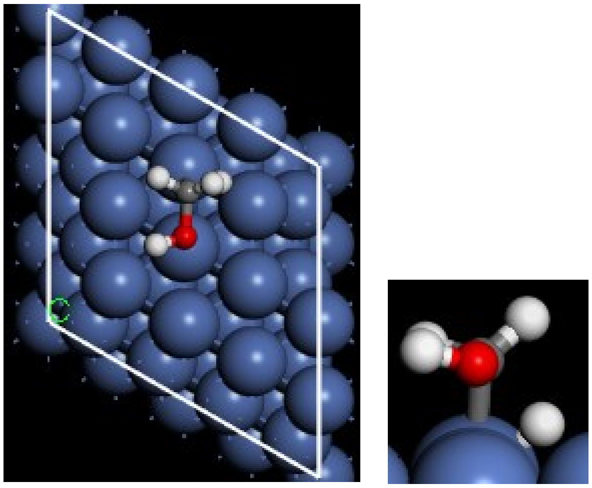

15. $CH_2OH^* \rightarrow CHOH^* + H^*$

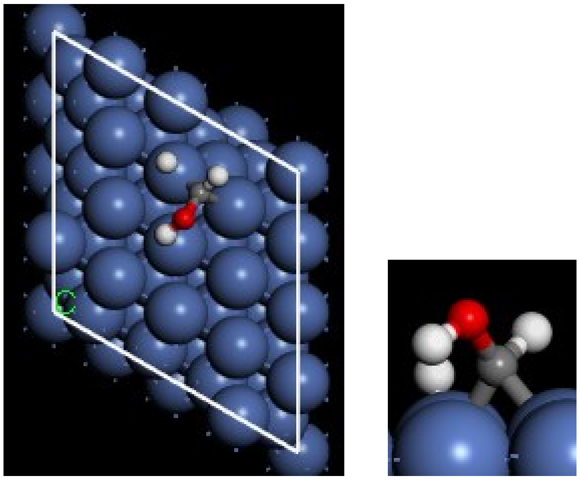

16. CHOH*→COH*+H*

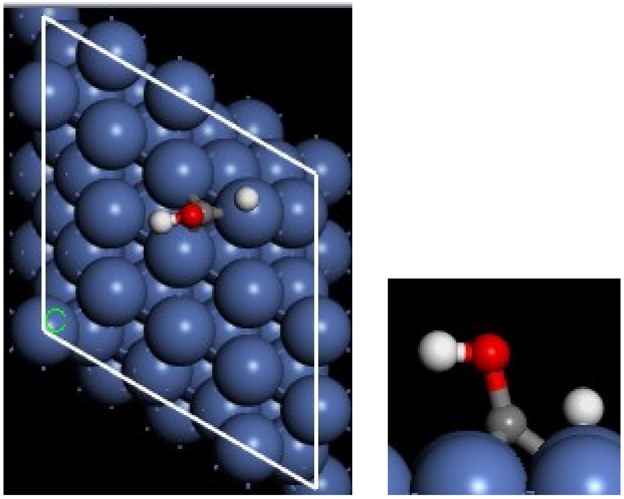

17. COH*→CO*+H*

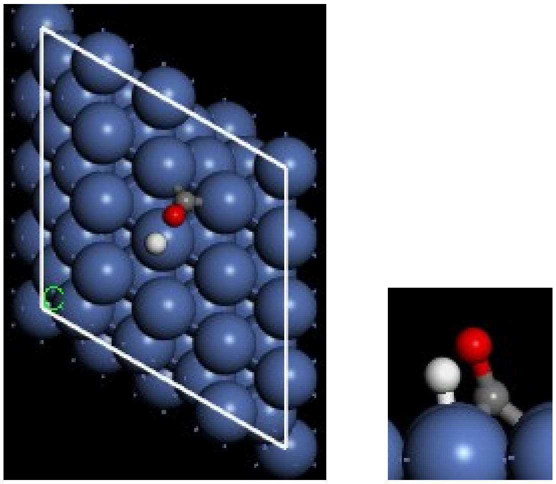

18. CH_3*+OH* →CH_3OH*

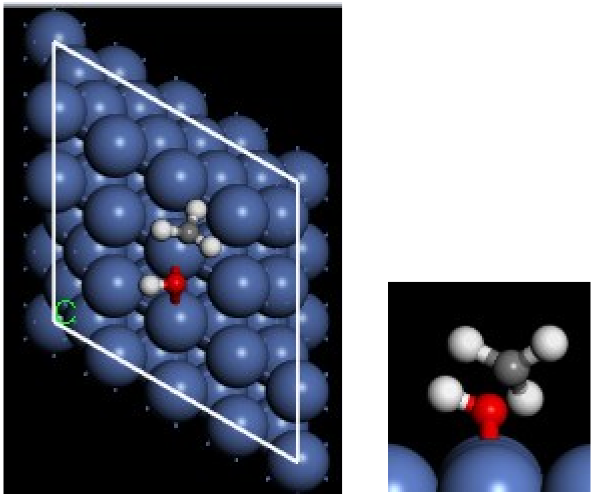

19. CH_2*+OH*→CH_2OH*

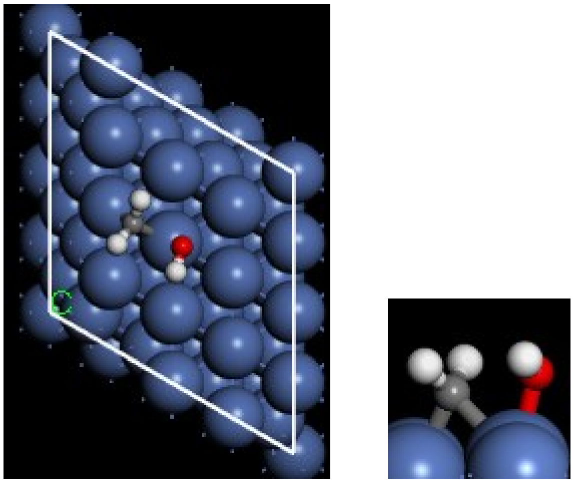

20. CH*+OH*→ CHOH*

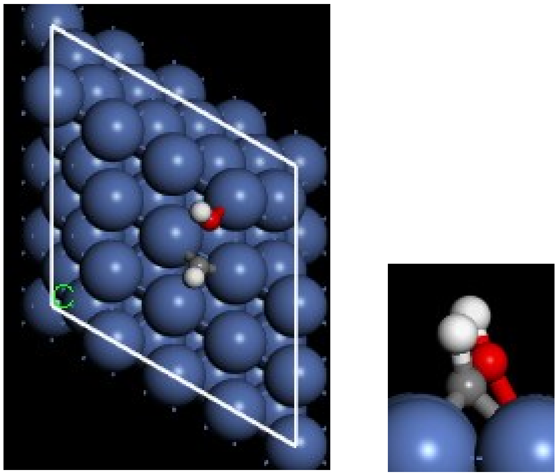

21. C*+OH*→COH*

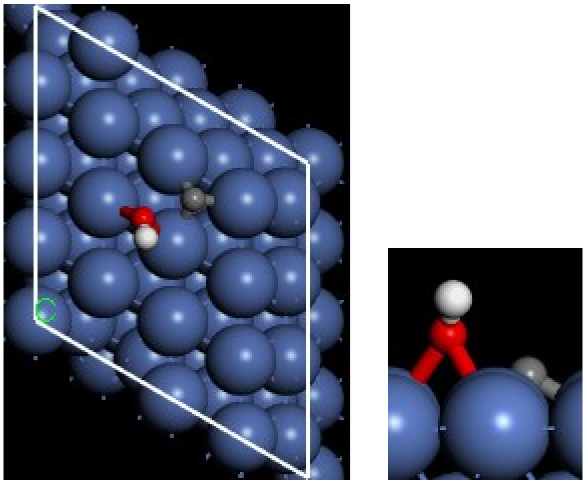

22. $CH_3O^* \rightarrow CH_2O^* + H^*$

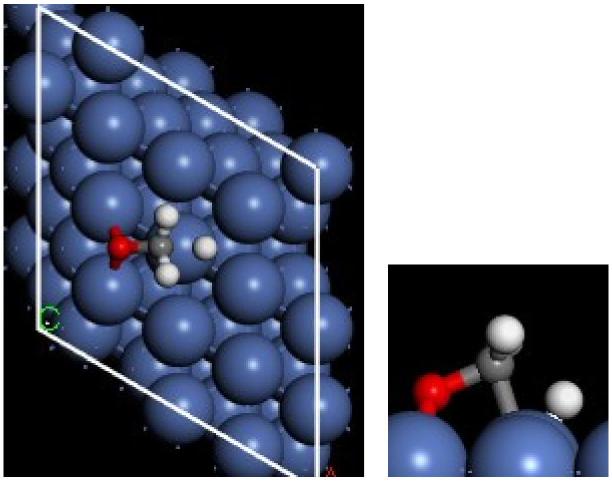

23. $CH_2O^* \rightarrow CHO^* + H^*$

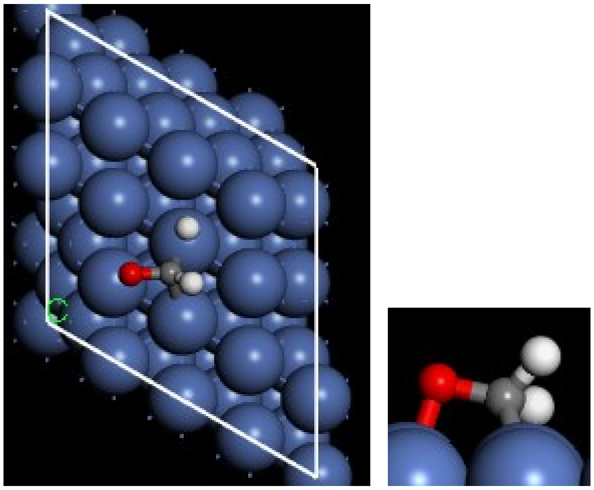

24. $CH_3^* + O^* \rightarrow CH_3O^*$

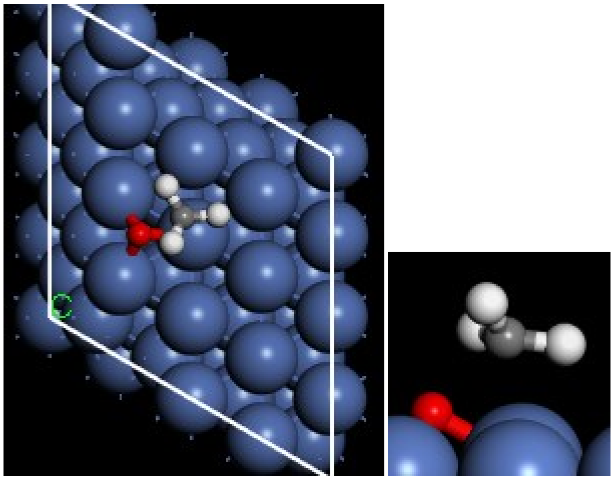

25. $CH_2^*+O^*\rightarrow CH_2O^*$

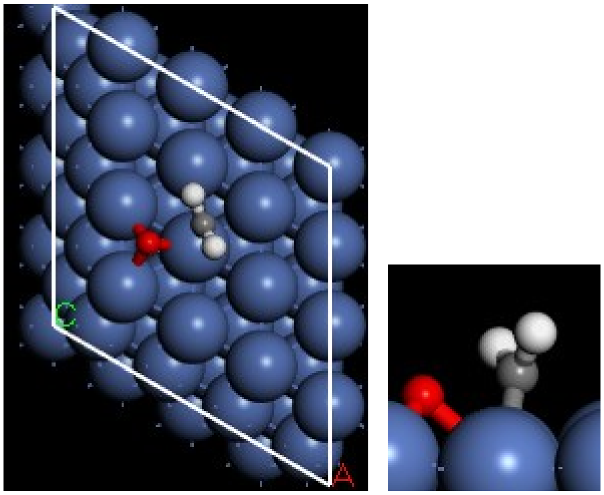

26. $CH^*+O^*\rightarrow CHO^*$

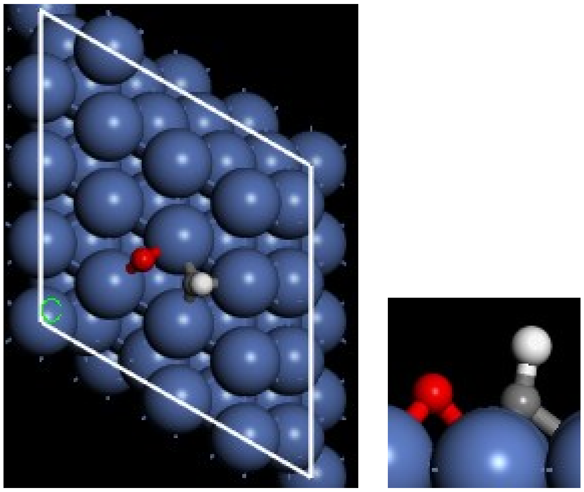

27. $C^*+O^*\rightarrow CO^*$

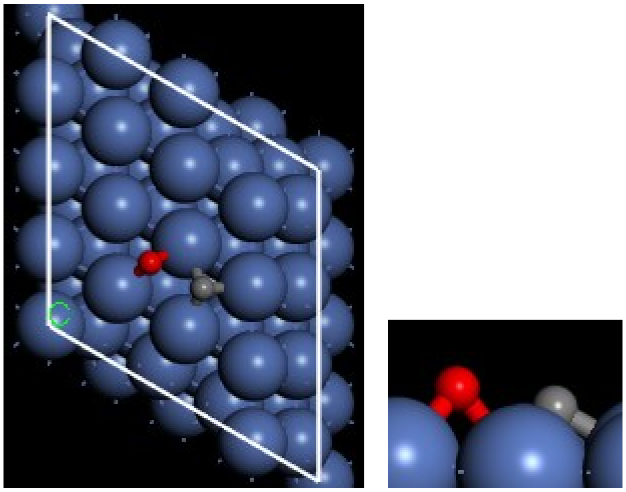

28. $CH_3OH^*+^* \rightarrow CH_3O^*+H^*$

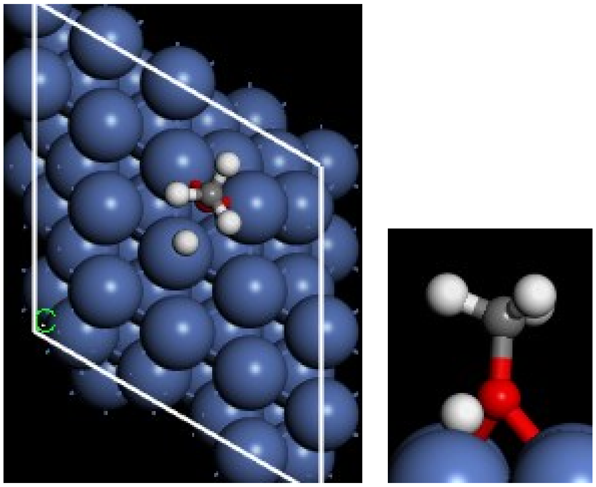

29. $CH_2OH^*+^* \rightarrow CH_2O^*+H^*$

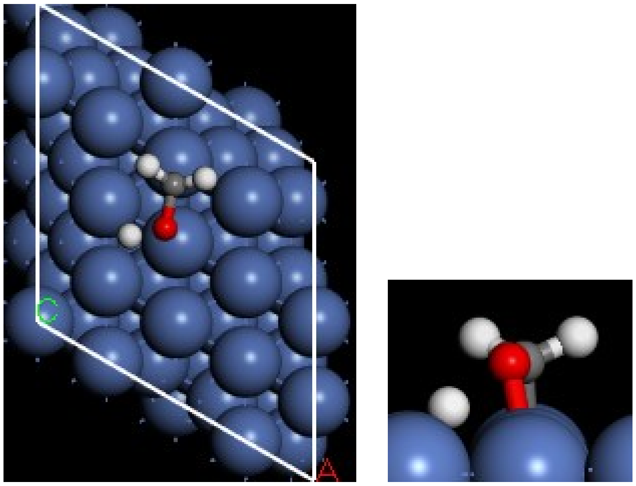

30. $CHOH^*+^* \rightarrow HCO^*+H^*$

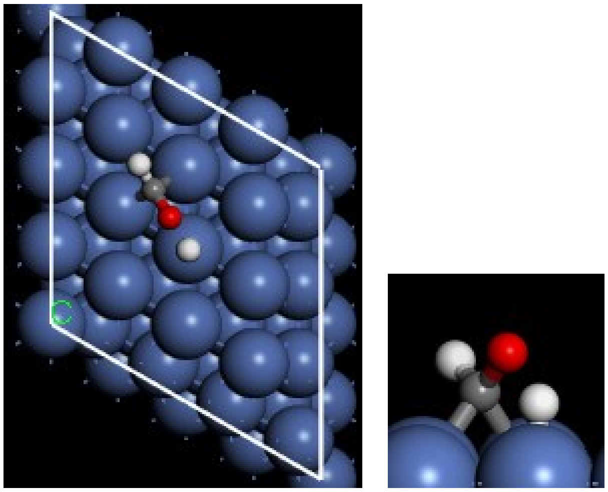

31. $O^*+H^*\rightarrow OH^*$

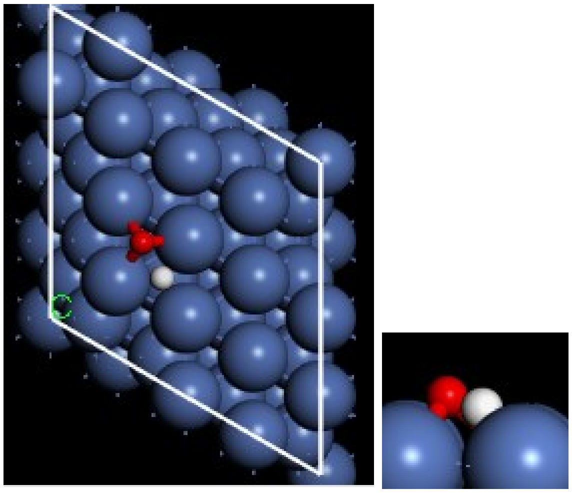

32. $OH^*+H^*\rightarrow H_2O^*$

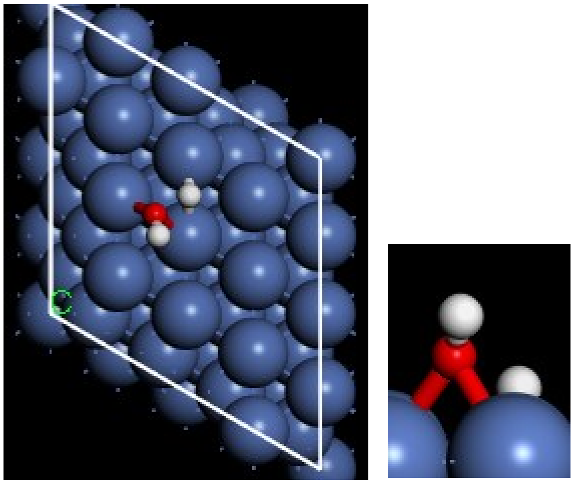

33. $H^*+H^*\rightarrow H_2$

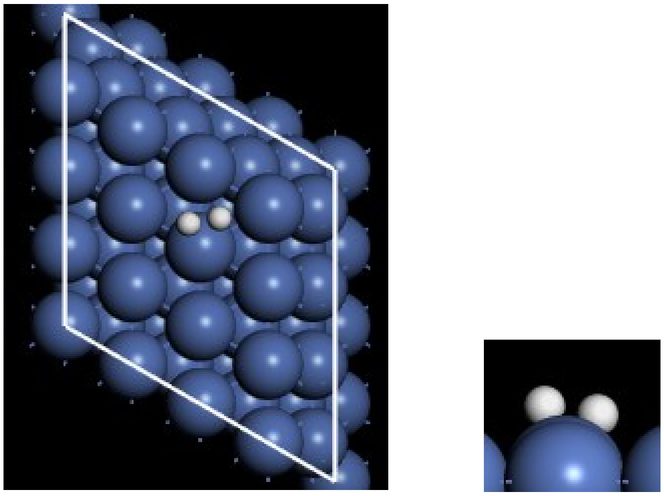

34. $OH^*+OH^*\rightarrow H_2O^*+O^*$

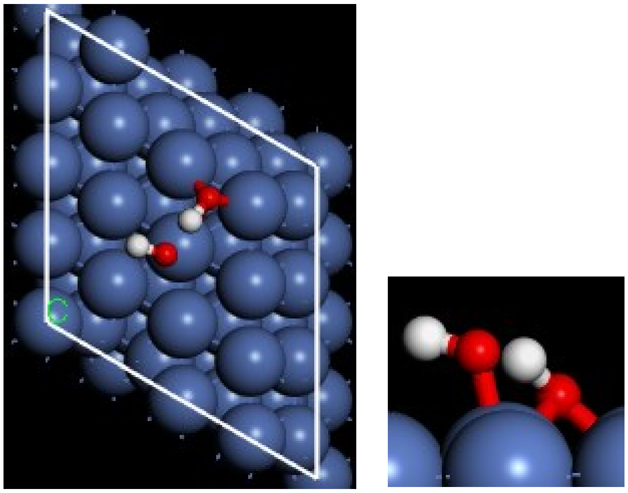

35. $CO_2^*+C^*\rightarrow 2CO^*$

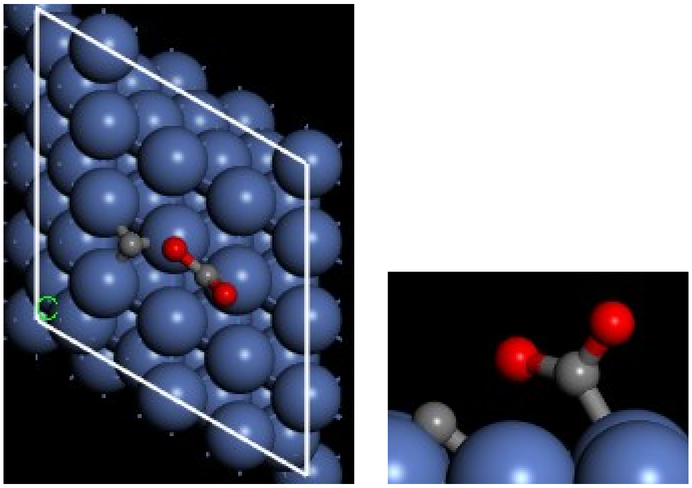

Intermediate Structures on NiB

1. CH_4

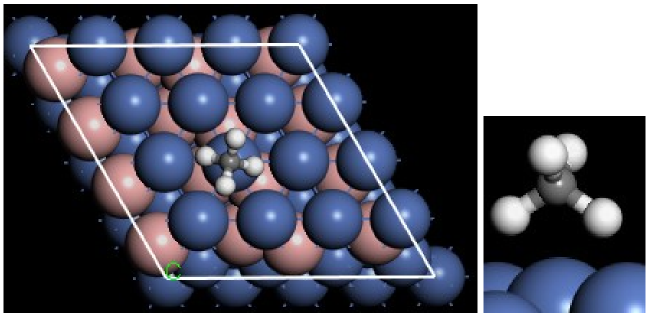

2. CH_3

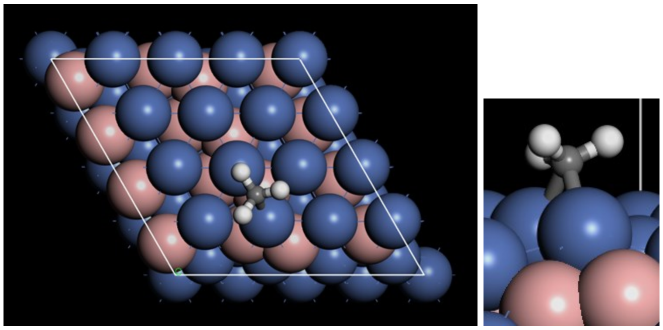

3. CH_2

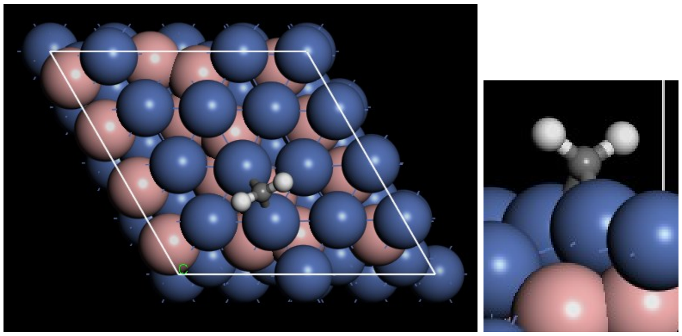

4. CH

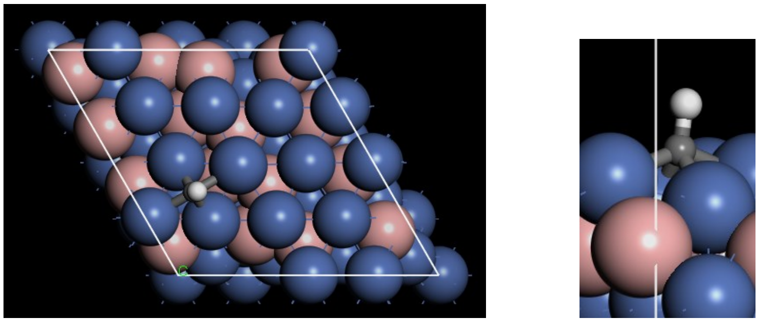

5. C

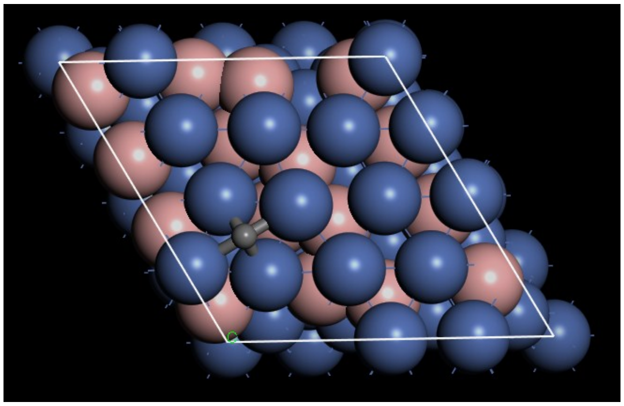

6. CO_2

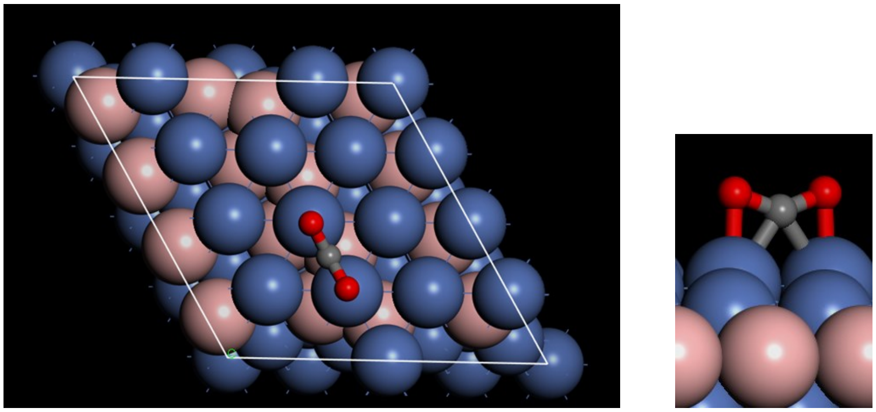

7. CO

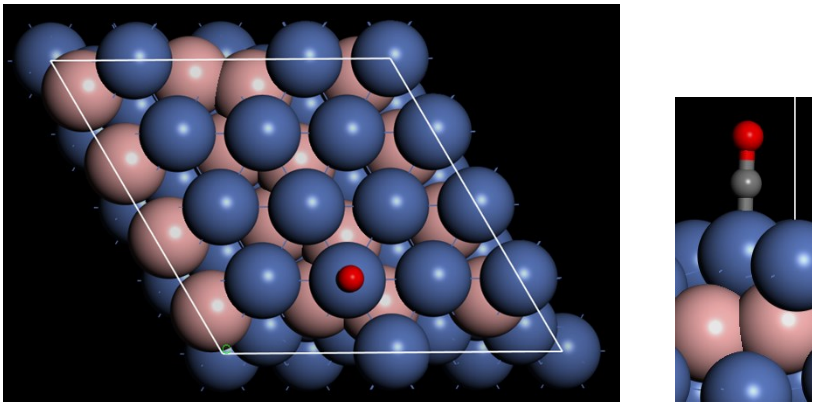

8. COOH

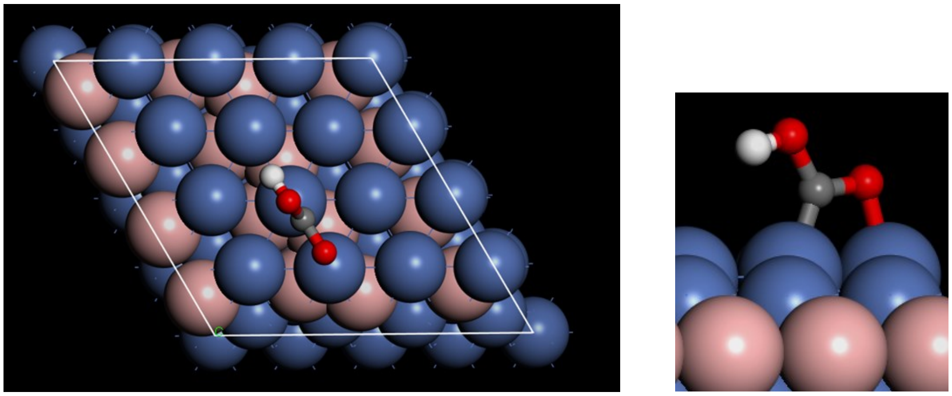

9. HCOO

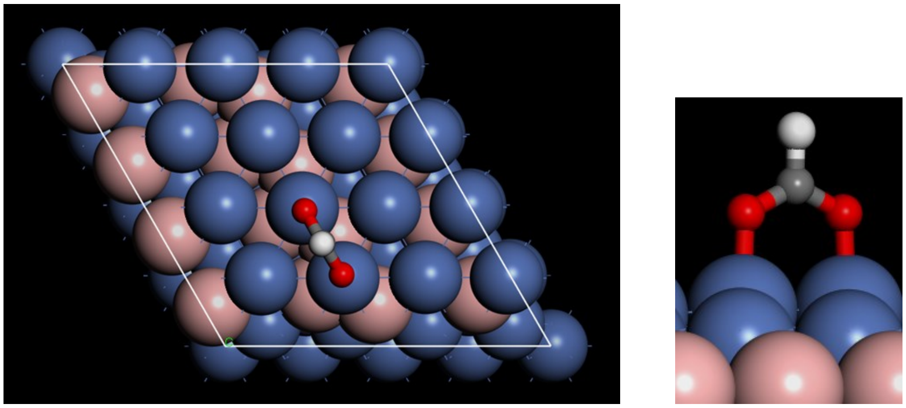

10. HCO

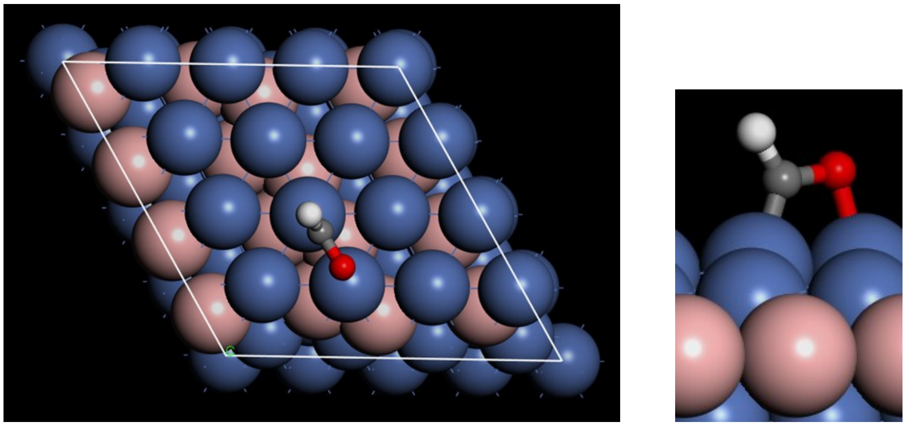

11. HCOOH

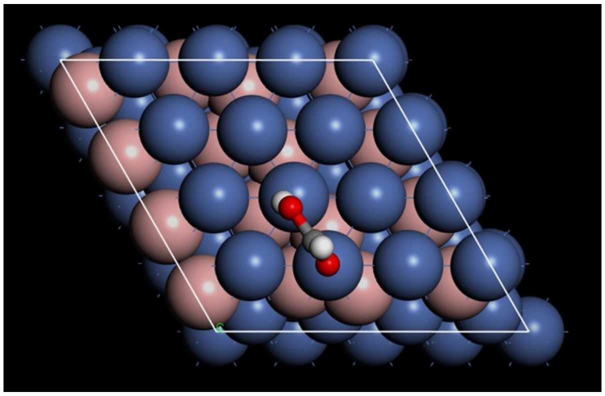

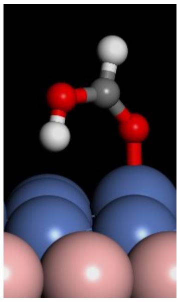

12. CH_3OH

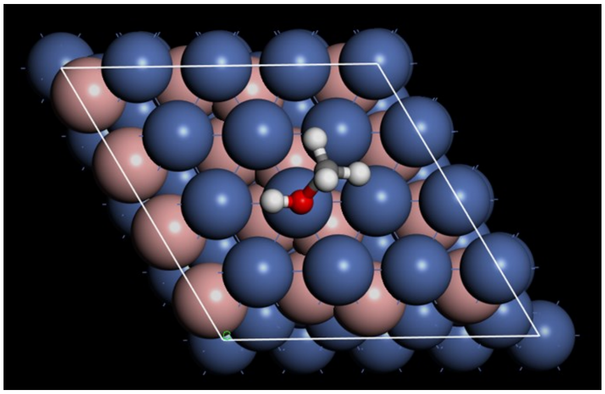

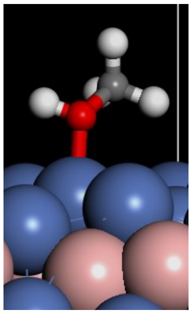

13. CH_2OH

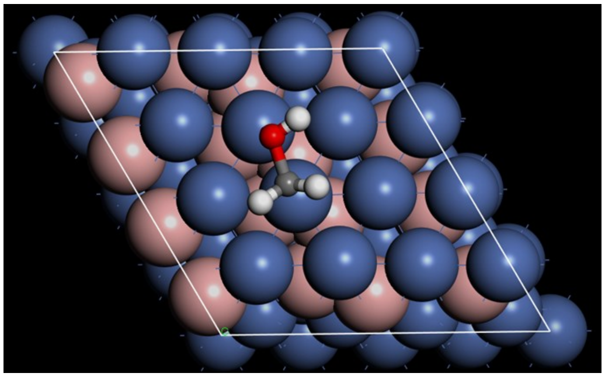

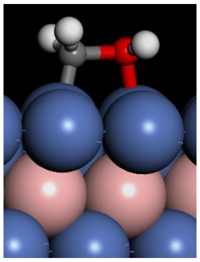

14. CHOH

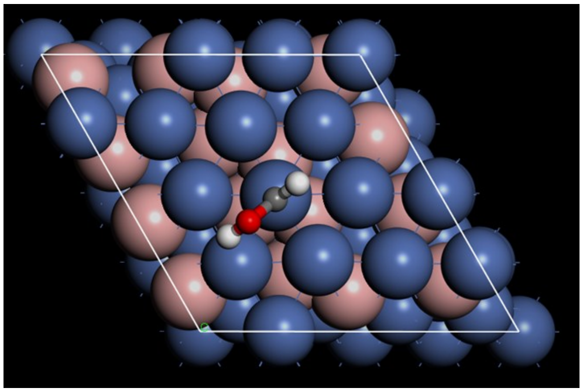

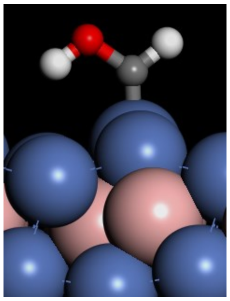

15. COH

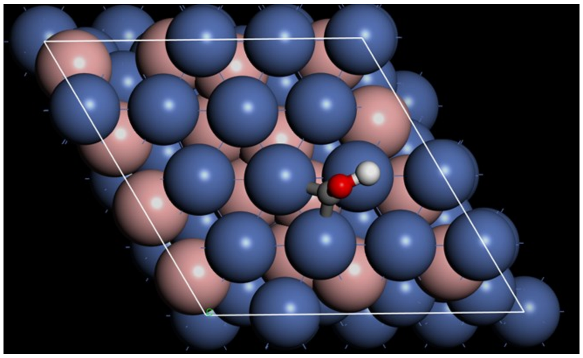

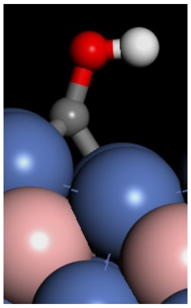

16. CH_3O

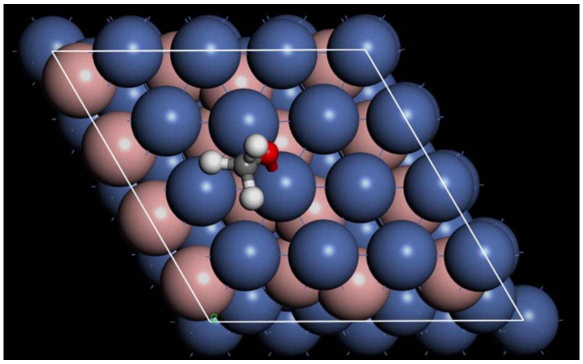

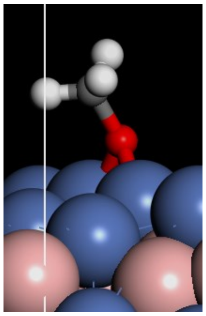

17. CH_2O

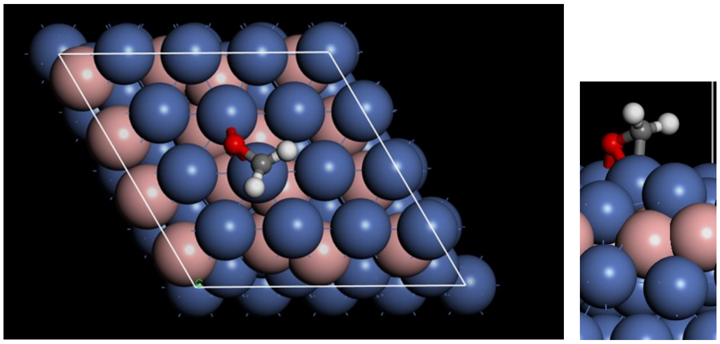

18. H_2O

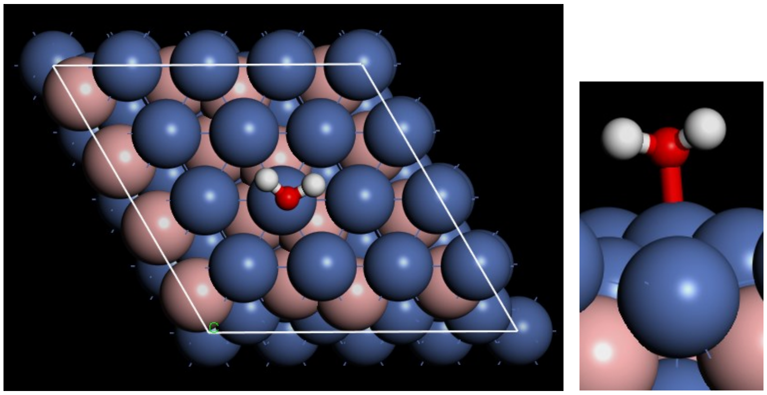

19. O

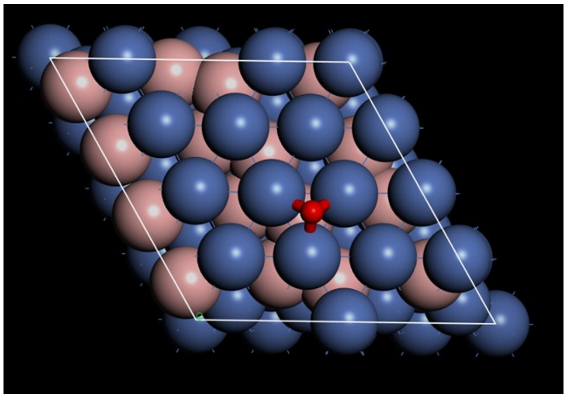

20. H

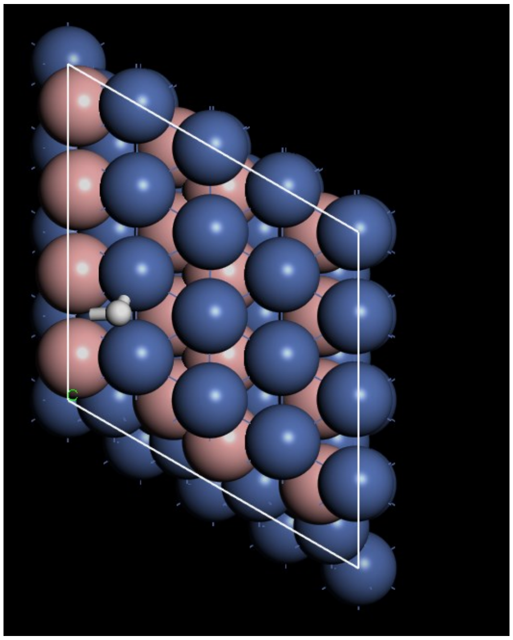

21. OH

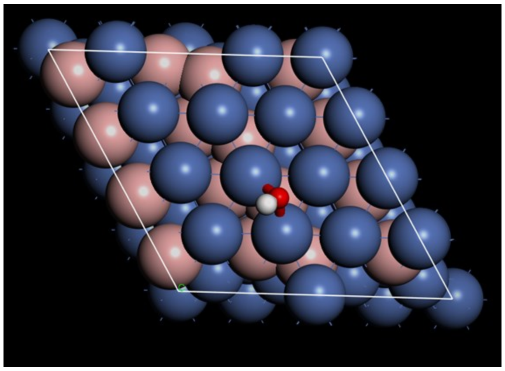

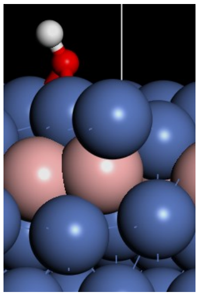

NiB----TS structures

1. $CH_4 \rightarrow CH_3^* + H^*$

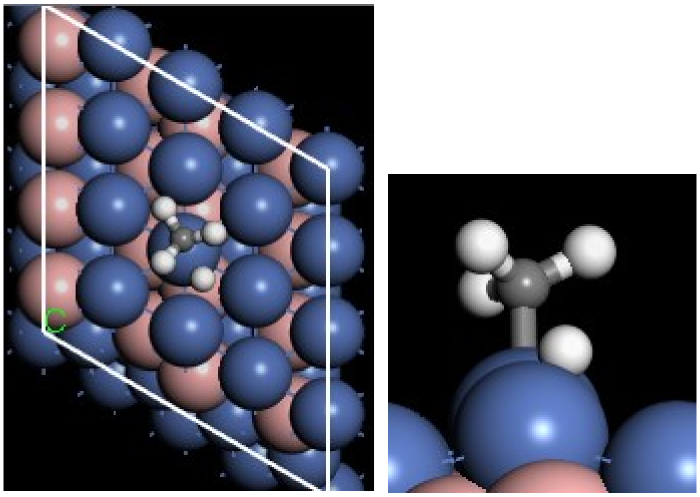

2. $CH_3^* \rightarrow CH_2^* + H^*$

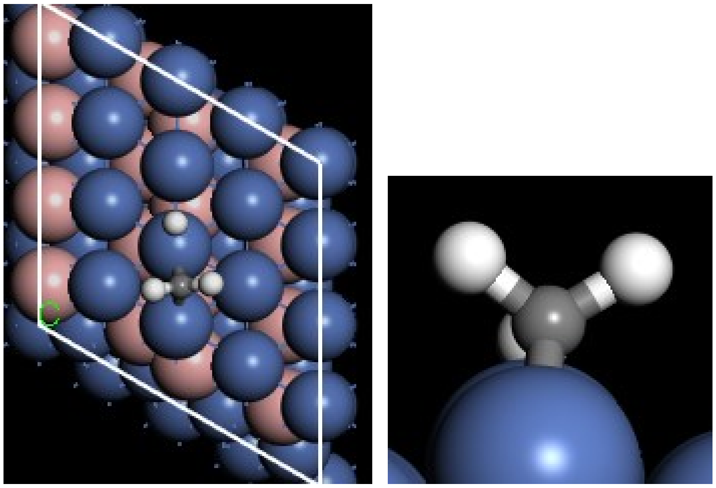

3. $CH_2^* \rightarrow CH^* + H^*$

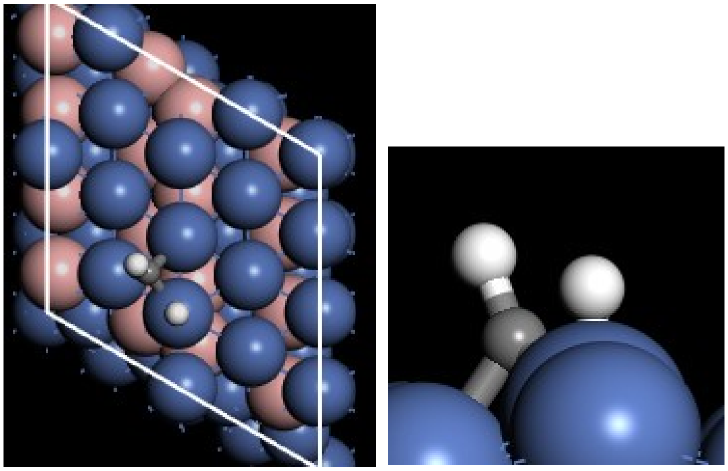

4. $CH^* \rightarrow C^* + H^*$

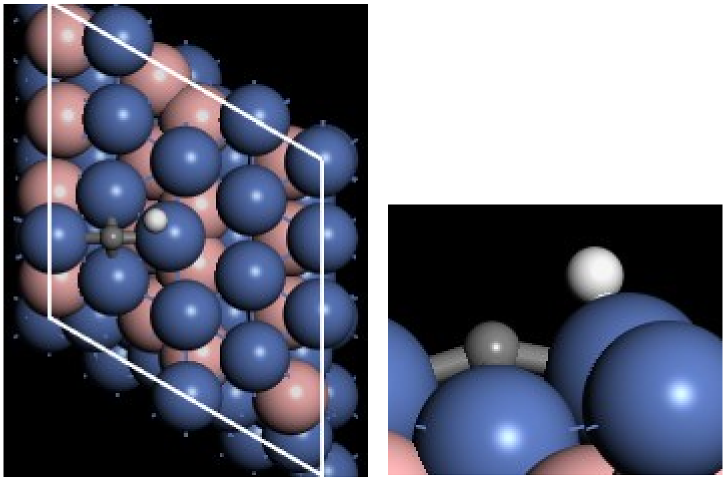

5. $CO_2^* \rightarrow CO^* + O^*$

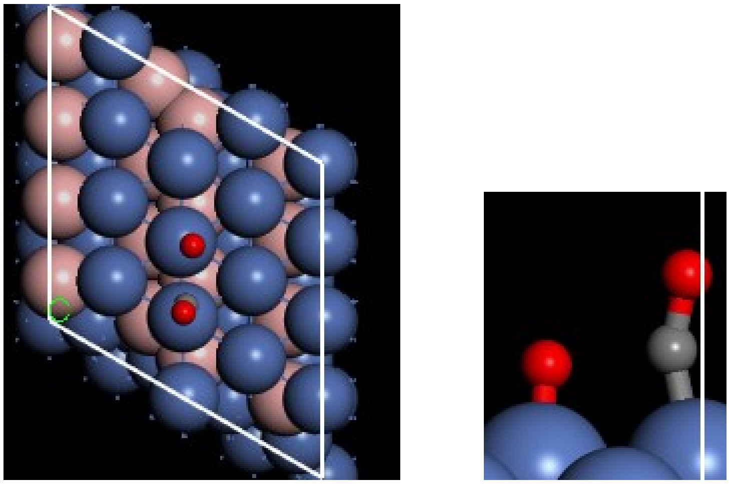

6. $CO_2^* + H^* \rightarrow COOH^*$

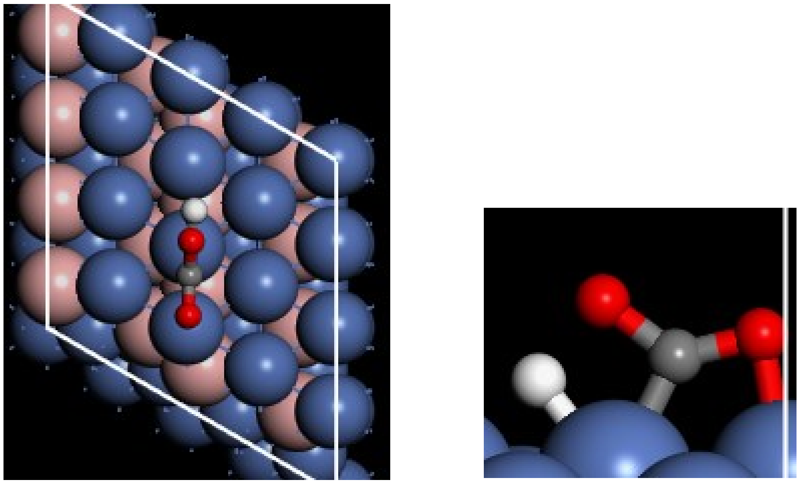

7. CO_2*+H*→HCOO*

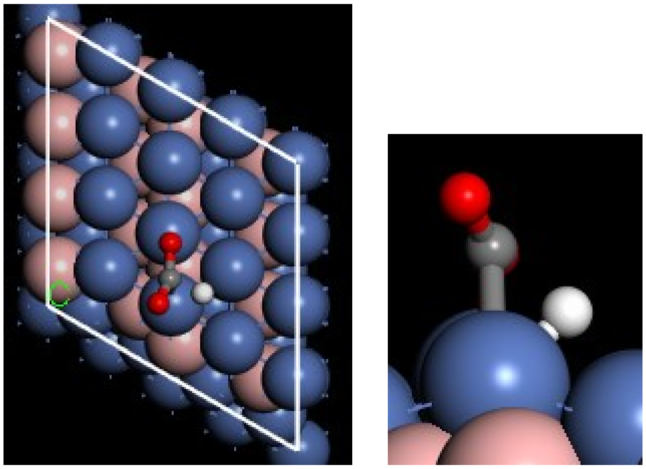

8. COOH*→CO*+OH*

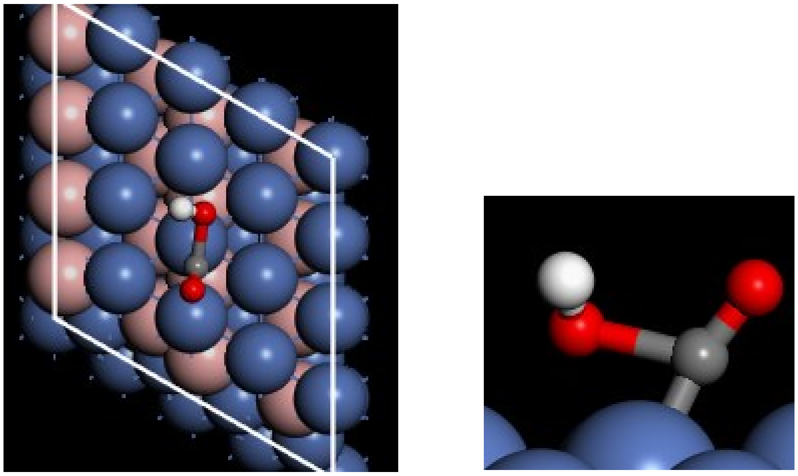

9. HCOO*→HCO*+O*

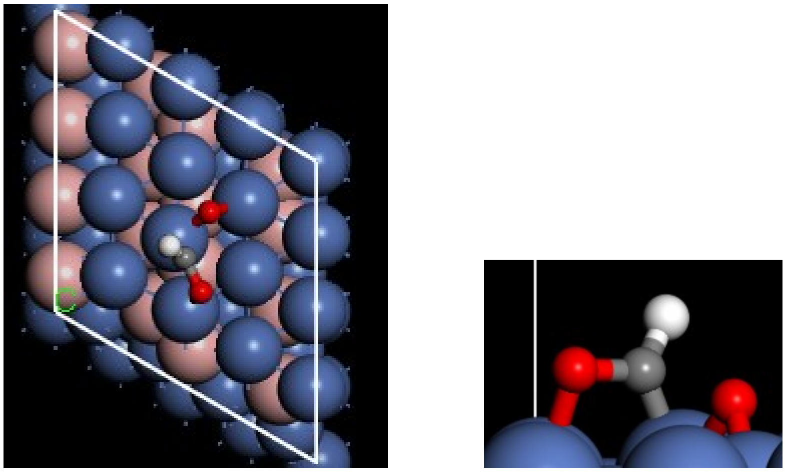

10. $HCO^{*} \rightarrow CO^{*} + H^{*}$

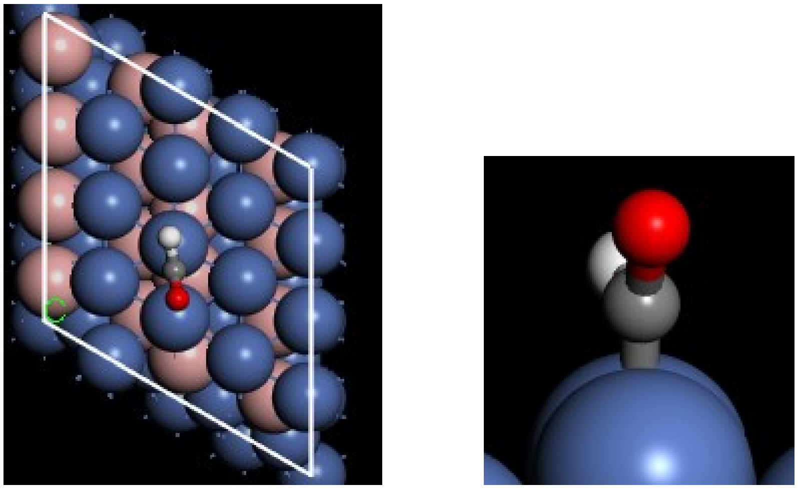

11. $COOH^{*} + H^{*} \rightarrow HCOOH^{*}$

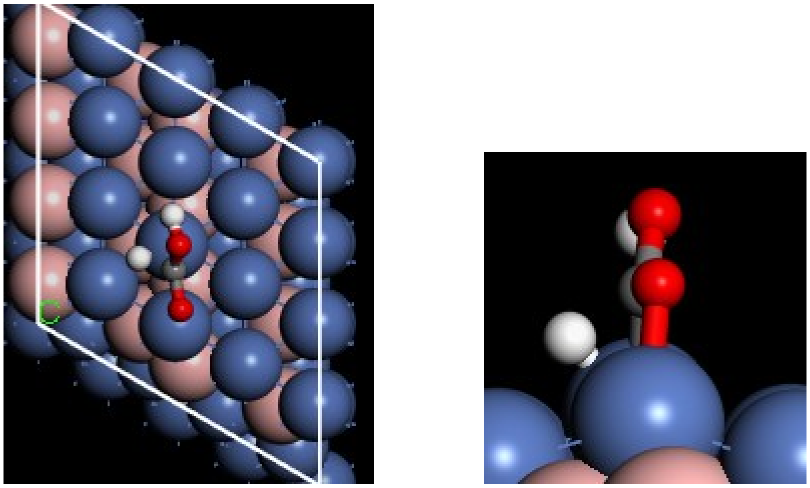

12. $HCOO^{*} + H^{*} \rightarrow HCOOH$

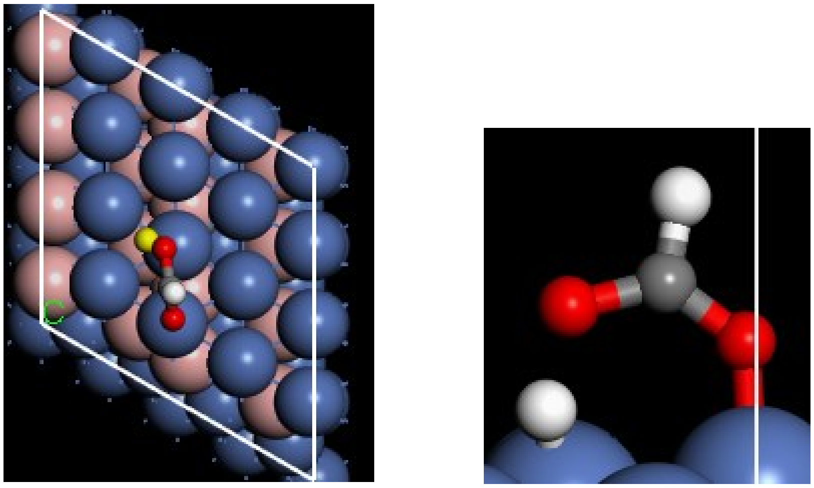

13. $HCOOH^* \rightarrow HCO^* + OH^*$

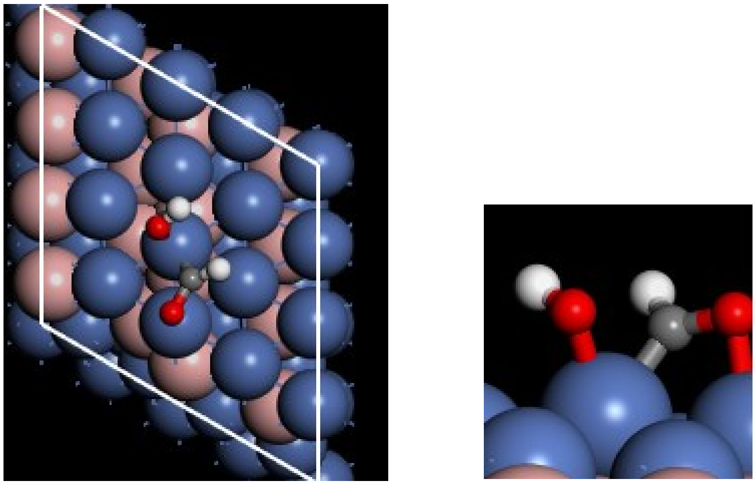

14. $CH_3OH^* \rightarrow CH_2OH^* + H^*$

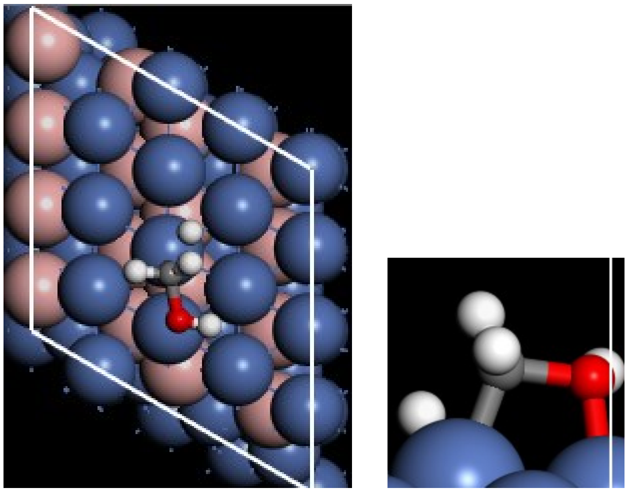

15. $CH_2OH^* \rightarrow CHOH^* + H^*$

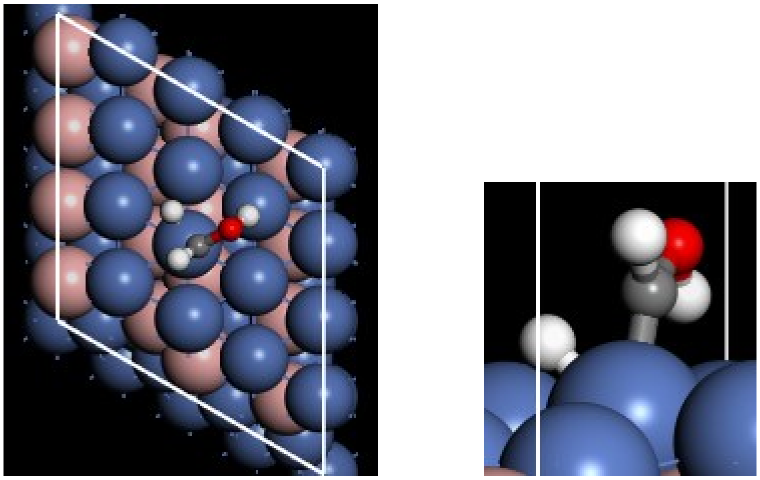

16. CHOH*→COH*+H*

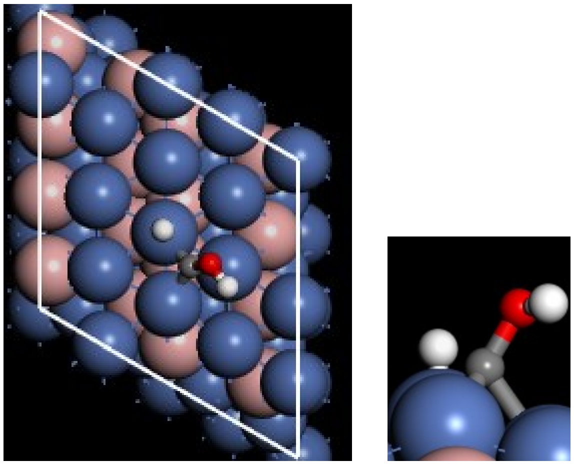

17. COH*→CO*+H*

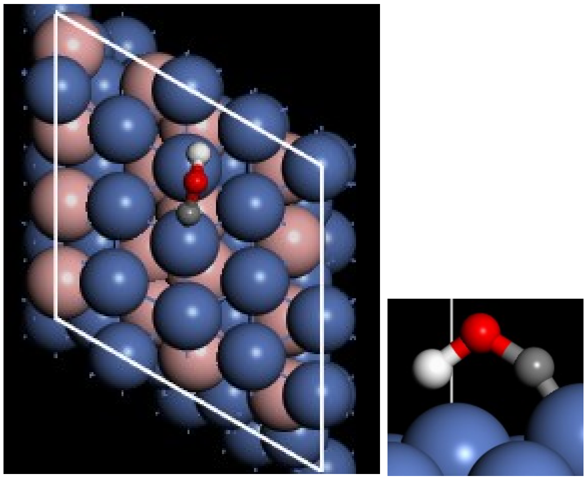

18. CH_3*+OH* →CH_3OH*

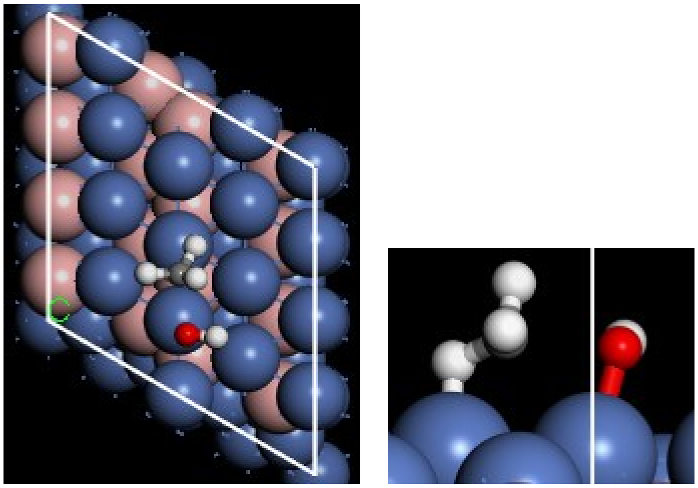

19. CH_2*+OH*→CH_2OH*

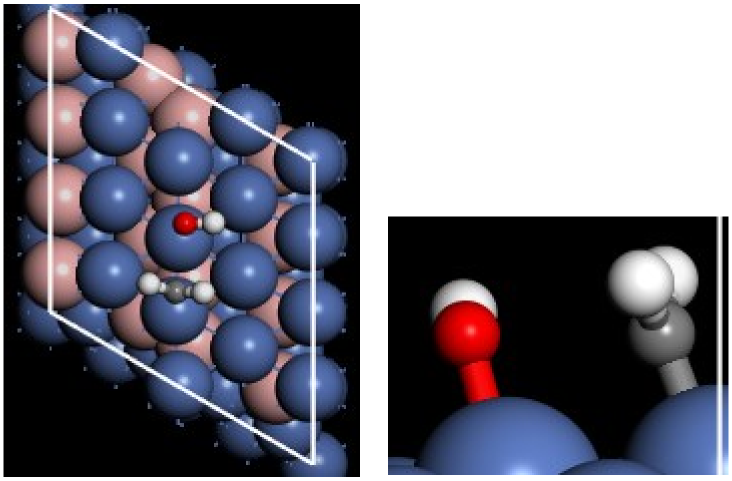

20. CH*+OH*→ CHOH*

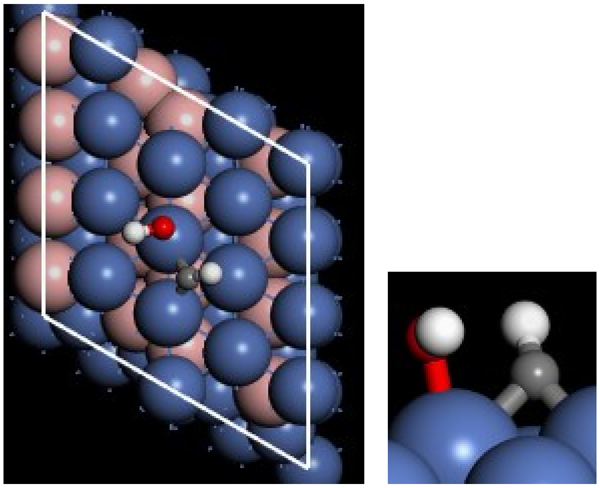

21. C*+OH*→COH*

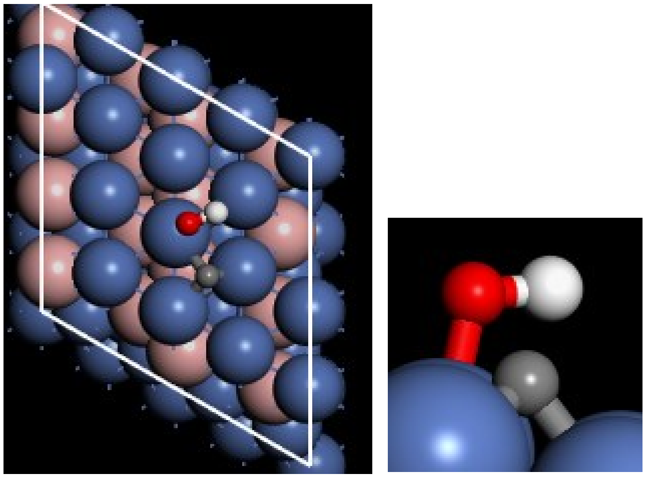

22. $CH_3O^* \rightarrow CH_2O^* + H^*$

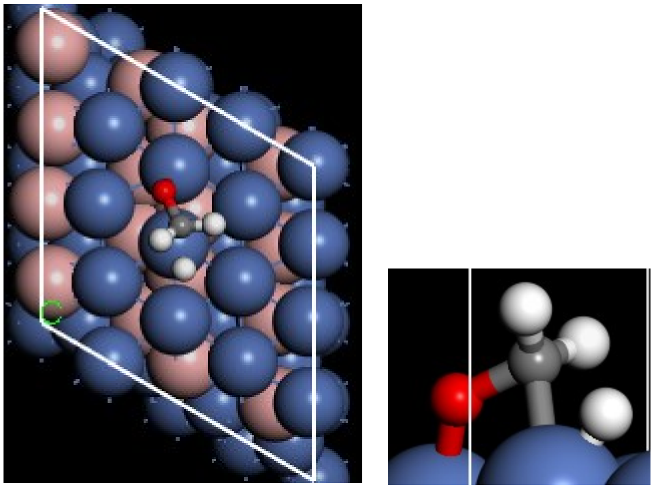

23. $CH_2O^* \rightarrow CHO^* + H^*$

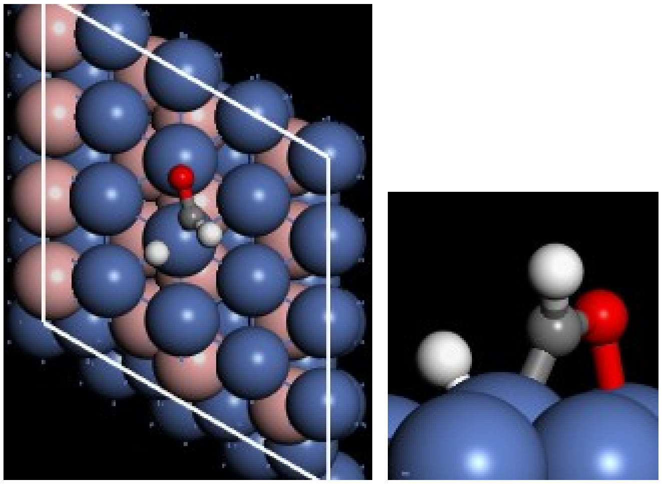

24. $CH_3^* + O^* \rightarrow CH_3O^*$

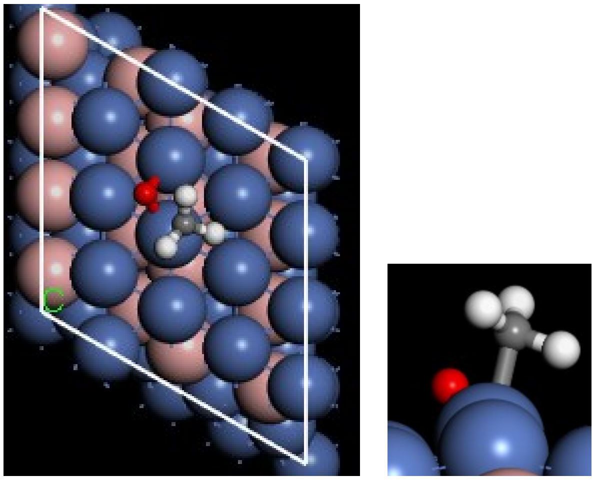

25. $CH_2^* + O^* \rightarrow CH_2O^*$

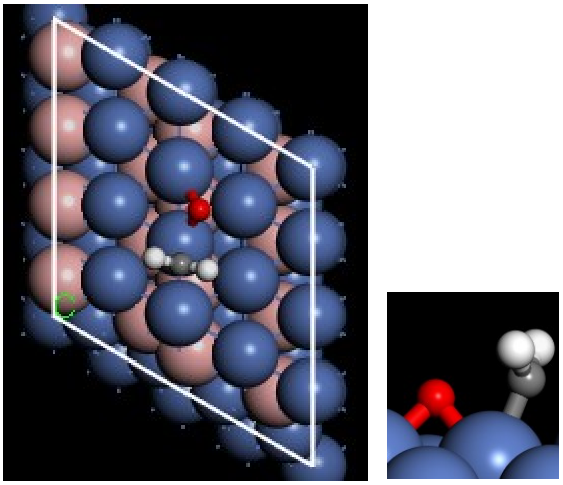

26. $CH^* + O^* \rightarrow CHO^*$

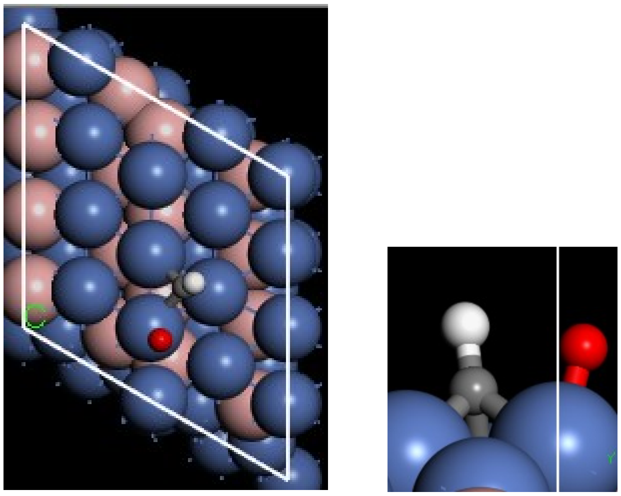

27. $C^* + O^* \rightarrow CO^*$

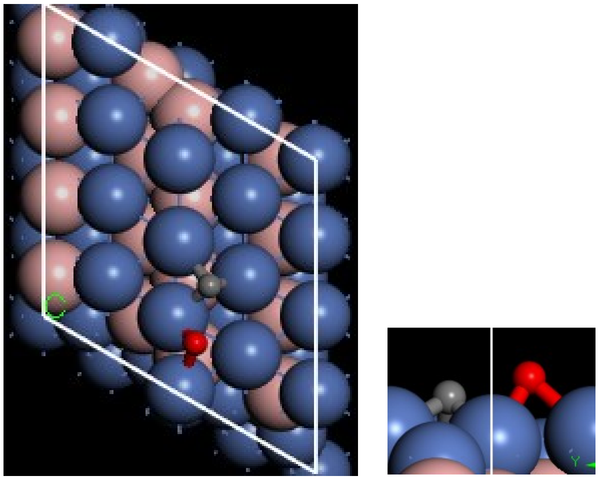

28. $CH_3OH^*+^* \rightarrow CH_3O^*+H^*$

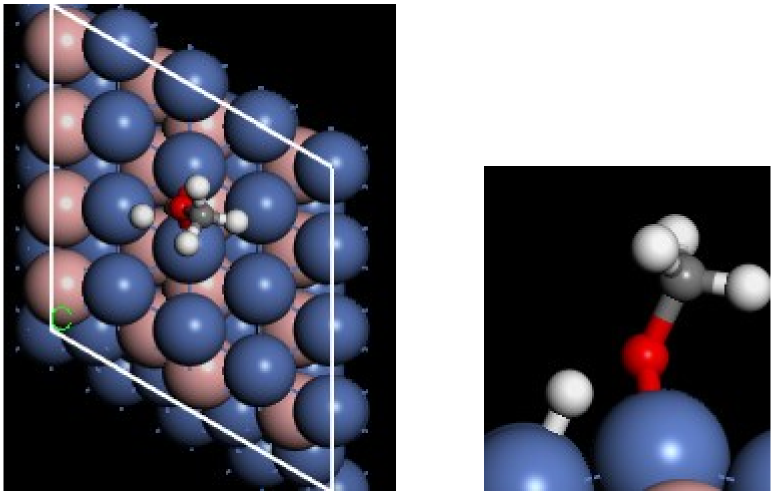

29. $CH_2OH^*+^* \rightarrow CH_2O^*+H^*$

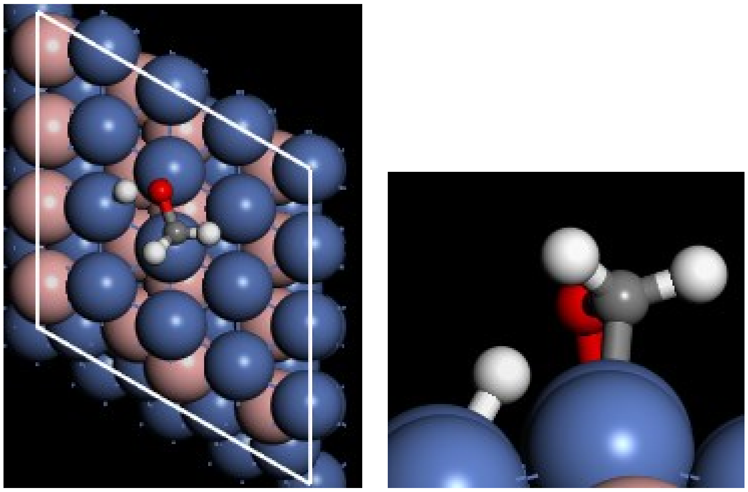

30. $CHOH^*+^* \rightarrow HCO^*+H^*$

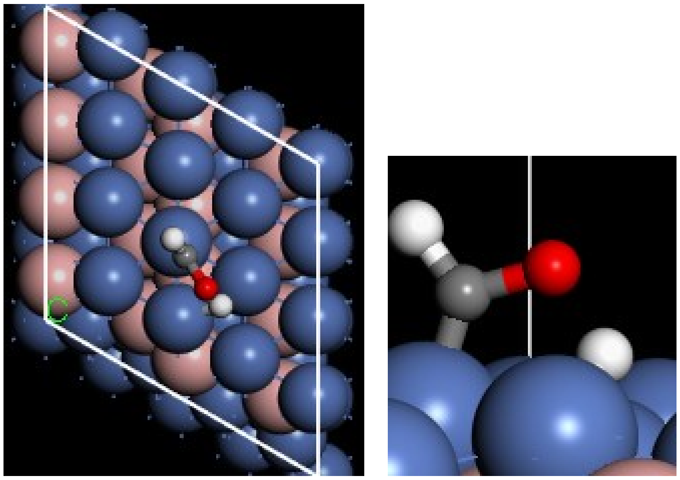

31. $O^* + H^* \rightarrow OH^*$

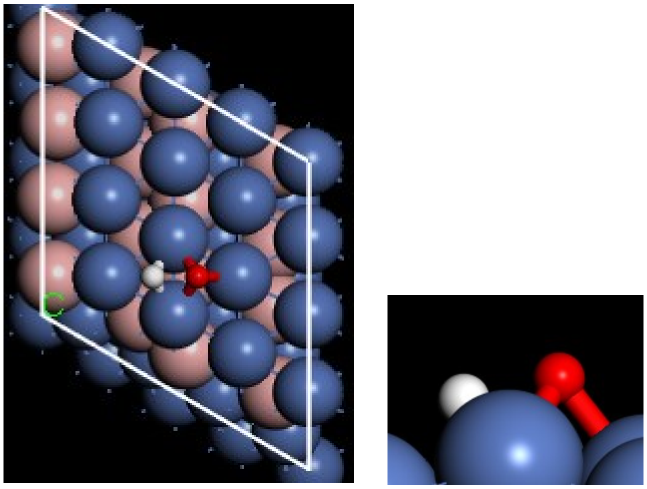

32. $OH^* + H^* \rightarrow H_2O^*$

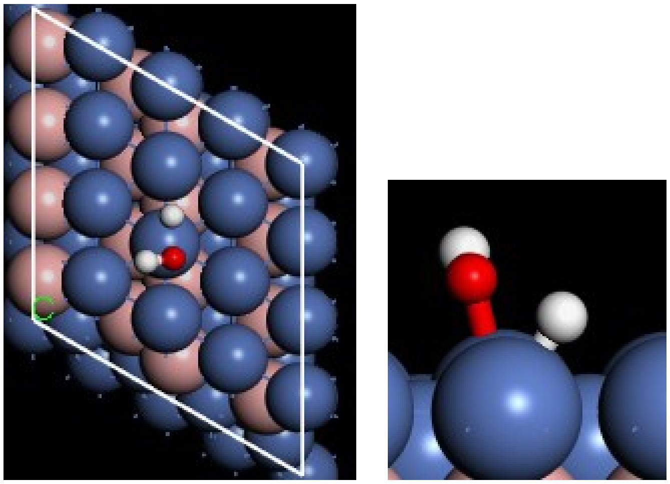

33. $H^* + H^* \rightarrow H_2$

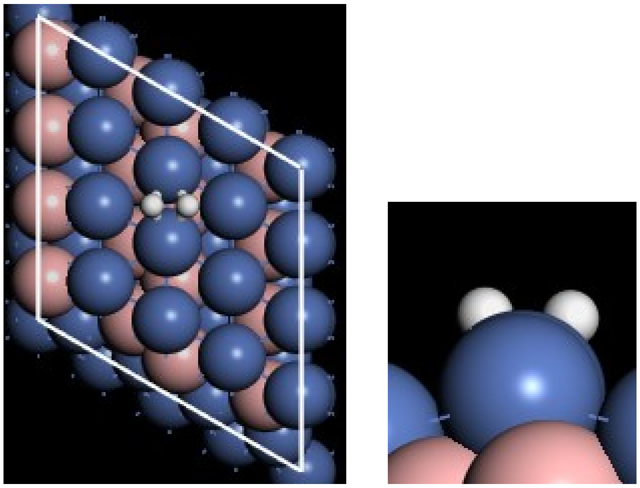

34. $OH^*+OH^*\rightarrow H_2O^*+O^*$

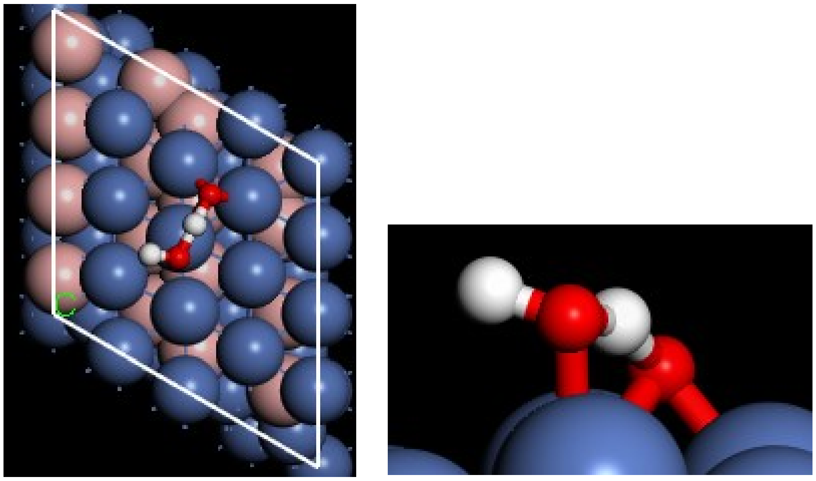

35. $CO_2^*+C^*\rightarrow 2CO^*$

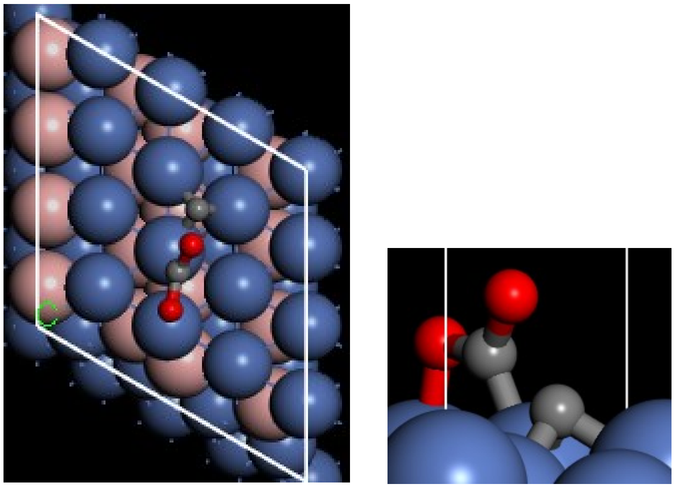

References

1 J. Xu and M. Saeys, *Chem. Eng. Sci.*, 2007, **62**, 5039–5041.

2 J. Xu, L. Chen, K. F. Tan, A. Borgna and M. Saeys, *J. Catal.*, 2009, **261**, 158–165.

3 J. Xu and M. Saeys, *J. Phys. Chem. C*, 2009, **113**, 4099–4106.

4 Q. T. Trinh, A. Banerjee, Y. Yang and S. H. Mushrif, *J. Phys. Chem. C*, 2017, **121**, 1099–1112.

5 J. S. Yoo, Z.-J. Zhao, J. K. Nørskov and F. Studt, *ACS Catal.*, 2015, **5**, 6579–6586.

6 R. D. Cortright and J. A. Dumesic, 2001, pp. 161–264.

7 Y.-A. Zhu, D. Chen, X.-G. Zhou and W.-K. Yuan, *Catal. Today*, 2009, **148**, 260–267.

8 S. G. Wang, D. B. Cao, Y. W. Li, J. Wang and H. Jiao, *J. Phys. Chem. B*, 2006, **110**, 9976–9983.

9 J. Li, E. Croiset and L. Ricardez-Sandoval, *Appl. Surf. Sci.*, 2014, **311**, 435–442.

10 S. G. Wang, D. B. Cao, Y. W. Li, J. Wang and H. Jiao, *Surf. Sci.*, 2009, **603**, 2600–2606.

11 T. Ogura, D. W. Blaylock, G. J. O. Beran and W. H. Green, *ACS Natl. Meet. B. Abstr.*, 2008, 4898–4908.

12 D. W. Blaylock, Y. A. Zhu and W. H. Green, *Top. Catal.*, 2011, **54**, 828–844.

13 T. Ogura, D. W. Blaylock, G. J. O. Beran and W. H. Green Jr., *ACS Natl. Meet. B. Abstr.*, 2008, 4898–4908.

14 J. Huang, X. Li, X. Wang, X. Fang, H. Wang and X. Xu, *J. CO2 Util.*, 2019, **33**, 55–63.

15 H. Yuan, X. Zhu, J. Han, H. Wang and Q. Ge, *J. CO2 Util.*, 2018, **26**, 8–18.

16 F. Che, J. T. Gray, S. Ha and J. S. McEwen, *ACS Catal.*, 2017, **7**, 551–562.

17 L. Maier, B. Schädel, K. H. Delgado, S. Tischer and O. Deutschmann, *Top. Catal.*, 2011, **54**, 845–858.

18 C. Fan, Y. A. Zhu, M. L. Yang, Z. J. Sui, X. G. Zhou and D. Chen, *Ind. Eng. Chem. Res.*, 2015, **54**, 5901–5913.

19 J. P. Perdew, K. Burke and M. Ernzerhof, *Phys. Rev. Lett.*, 1996, **77**, 3865–3868.

20 B. Hammer, L. Hansen and J. Nørskov, *Phys. Rev. B*, 1999, **59**, 7413–7421.

21 Z. Han, Z. Yang and M. Han, *Appl. Surf. Sci.*, 2019, **480**, 243–255.

22 V. C. H. Kroll, H. M. Swaan, S. Lacombe and C. Mirodatos, *J. Catal.*, 1996, **164**, 387–398.

23 J. Li, E. Croiset and L. Ricardez-Sandoval, *Appl. Surf. Sci.*, 2014, **311**, 435–442.

24 K. Delgado, L. Maier, S. Tischer, A. Zellner, H. Stotz and O. Deutschmann, *Catalysts*, 2015, **5**, 871–904.

25 S. Wang, *Ind. Eng. Chem. Res.*, 1999, **38**, 2615–2625.

26 J. A. Dumesic, *J. Catal.*, 1999, **185**, 496–505.

27 A. Nandini, K. K. Pant and S. C. Dhingra, *Appl. Catal. A Gen.*, 2006, **308**, 119–127.